Tectonophysics 496 (2010) 28–43

Contents lists available at ScienceDirect

Tectonophysics

journal homepage: www.elsevier.com/locate/tecto

The role of footwall deformation and denudation in controlling cooling age patterns of detachment systems: An application to the Kongur Shan extensional system in the Eastern Pamir, China

Alexander C. Robinson [a,*], An Yin [b,c,1], Oscar M. Lovera [b,2]

[a] Department of Earth and Atmospheric Sciences, University of Houston, Houston, TX, 77204, United States
[b] Department of Earth and Space Sciences, University of California, Los Angeles, CA, 90095-1567, United States
[c] Institute of Geophysics and Planetary Physics, University of California, Los Angeles, CA, 90095-1567, United States

ARTICLE INFO

Article history:
Received 25 May 2010
Received in revised form 6 October 2010
Accepted 9 October 2010
Available online 14 October 2010

Keywords:
Thermal model
Pamir
Kongur Shan
Thermochronology

ABSTRACT

Determining the relationship between deformation and exhumation history in the footwall rocks of major low-angle normal faults (i.e., detachment faults) provides a way to quantify different models of continental extension. Although pressure–temperature–time (*P*–*T*–*t*) datasets are commonly used to infer magnitude and rates of slip across detachment faults, correct use of these datasets requires a sound understanding of coupling effects between footwall deformation and advection of isotherms on the distribution of cooling ages. In this study we present thermo-kinematic modeling results which examine the relationship between different footwall kinematic models, erosion, and the spatial distribution of muscovite and biotite $^{40}Ar/^{39}Ar$ cooling ages. Our results show that large magnitudes of footwall erosion during normal faulting significantly affect cooling age patterns as footwall rocks at different distances from the fault surface pass through different thermal gradients. We apply our modeling results to simulating muscovite and biotite cooling-age patterns from the footwall of the Cenozoic Kongur Shan normal fault system in the Pamir. Previous studies had interpreted a documented ~5-fold increase in cooling rate at ~2 Ma to indicate an increase in exhumation rate during the Quaternary. However, our results show that the observed cooling age patterns and increase in cooling rate can be produced by a constant exhumation rate over the last 7 Ma due to the effect of changes in the rate of isotherm advection during exhumation.

1. Introduction

Understanding the dynamics of continental tectonics requires determination of the spatial and temporal evolution of particle paths within a tectonic system. The problem can be readily addressed in deformed sedimentary terranes where primary bedding and syn-tectonic sedimentary strata allow one to track in detail the spatial and temporal evolution of deformation across the relevant tectonic systems (e.g., Suppe and Medwedeff, 1990; Xiao and Suppe, 1992). However, tracking the deformation history and strain paths in high-grade metamorphic terranes has been exceedingly challenging due to a general lack of suitable strain markers to determine finite strain and strain history as a result of obliteration of primary geologic features by metamorphism and penetrative ductile deformation. A classic example of this problem is the evolution of high-grade mylonitic gneisses exposed in the footwalls of major detachment faults (e.g. Lister and Davis, 1989). Although competing kinematic models have been proposed for detachment fault evolution (e.g., Spencer, 1984; Buck, 1988; Wernicke and Axen, 1988; Lister and Davis, 1989; Yin and Dunn, 1992), critically testing these has proven difficult due to the lack of continuously traceable strain markers to determine footwall strain paths and strain histories (e.g., Manning and Bartley, 1994; Axen and Bartley, 1997). In the past, thermochronology has been used to determine the kinematic and thermal evolution of major detachment faults (e.g. Richard et al., 1990; John and Foster, 1993; Harrison et al., 1995; Wells et al., 2000; Carter et al., 2004, 2006; Brichau et al., 2008), and comparison of spatially distributed cooling ages to simulations by thermo-kinematic models has yielded a wealth of insight into the slip rate, original fault geometry, and kinematic evolution of detachment fault systems (Ruppel et al., 1988; e.g. Grasemann and Mancktelow, 1993; Harrison et al., 1995; Ketcham, 1996; Kapp et al., 2005). The above studies tend to emphasize the thermal evolution of particles along the detachment fault alone, and when they did deal with footwall deformation only the simplest cases such as simple shear and pure-shear strain histories were considered (e.g., Buck et al., 1988; Ruppel et al., 1988; Ketcham, 1996).

To address more complicated kinematic scenarios, we first use forward modeling to investigate the relationship between the

* Corresponding author. Tel.: +1 713 893 1316.
E-mail addresses: acrobinson@uh.edu (A.C. Robinson), yin@ess.ucla.edu (A. Yin), lovera@ess.ucla.edu (O.M. Lovera).
[1] Tel.: +1 310 825 8752.
[2] Tel.: +1 310 206 2657.

0040-1951/$ – see front matter © 2010 Elsevier B.V. All rights reserved.
doi:10.1016/j.tecto.2010.10.003

kinematics of detachment footwall deformation, *P–T–t* paths of footwall particles, and $^{40}Ar/^{39}Ar$ cooling age patterns for biotite and muscovite as a function of distance from the fault surface in cross-section view. We start by considering different kinematic scenarios of detachment fault footwall evolution where all particles exposed at the surface were exhumed along the same strain path directly beneath the detachment surface and with no erosion of material at the surface. We then explore the effect of heterogeneously distributed erosion across detachment footwalls which results in particles exposed at the surface being exhumed along strain paths at various distances from the detachment surface. The latter effect has been shown to be important in extensional settings for interpreting low-temperature thermochronologic data (e.g. apatite U–Th/He and fission track ages) (Ehlers et al., 2001, 2003; Ehlers and Farley, 2003). However, this effect has not been explored for higher temperature thermochronometers in extensional settings (e.g. muscovite and biotite $^{40}Ar/^{39}Ar$). We apply the insights gained from these forward numerical experiments to the Cenozoic Kongur Shan extensional system in the eastern Pamir at the western end of the Indo-Asian collision zone (Arnaud et al., 1993; Brunel et al., 1994; Yin and Harrison, 2000; Robinson et al., 2004, 2007).

2. Thermal model

2.1. Method

In this study, we solve the heat-transport equation using a two-dimensional explicit finite-difference method. The heat-transport equation is written as

$$\frac{\partial T}{\partial t} = \kappa\nabla^2 T - V\cdot\nabla T + \frac{A_o}{\rho c} \tag{1}$$

where T is temperature, t is time, κ is thermal diffusivity, V is velocity, A_o is heat generation, ρ is density, and c is heat capacity. In our numerical scheme, the evolution of temperature distributions was calculated at a discrete increment of particle motion using a prescribed velocity field across the footwall and a prescribed slip rate on the fault. The method tracks thermal relaxation between discrete steps of particle motion. The crustal section in the model is treated as a homogeneous medium with a uniform thermal conductivity of 2.25 W m^{-1} K^{-1}. The initial geothermal gradient in the crust is calculated from equations 4–31 of Turcotte and Schubert (2002) for a one-dimensional steady state geothermal gradient:

$$T = T_0 + \frac{q_m y}{k} + \frac{(q_0 - q_m)h_r}{k}\left(1 - e^{-y/h_r}\right) \tag{2}$$

where T_0 is the surface temperature, q_m is the heat flux from the mantle, q_0 is the surface heat flow, y is the depth at a given point, k is the thermal conductivity, and h_r is the depth from the surface of effective internal heating. Thermal parameters were kept constant for all models (Table 1), with only the description of the velocity field varying.

Table 1
Numerical model parameters.

Model input value	
Material properties	
Surface heat flux (q_0)	75 mW/m^2
Mantle heat flux (q_m)	35 mW/m^2
Shear Stress	40 MPa
Thermal conductivity (k)	2.25 W/m/K
Surface temperature	0 °C
Heat generation (A_0)	10^{-6} W/m^3
Numerical properties	
Width of fault shear zone	0.4 km
Model domain size (z, x)	35 km, variable

For each velocity model we assume a fixed, rigid hanging wall (region I, Fig. 1) with no subsidence or basin formation. The footwall moves with a velocity field $V(x, y) = (u\ (x, y), v(x, y))$, where u and v are the velocity components in the x (horizontal) and y (vertical) directions. The velocity components are related to strain-rate tensor by

$$\begin{aligned}\dot{\varepsilon}_{xx} &= \frac{\partial u}{\partial x}\\ \dot{\varepsilon}_{yy} &= \frac{\partial v}{\partial y}\\ \dot{\varepsilon}_{xy} &= \frac{1}{2}\left(\frac{\partial u}{\partial y} + \frac{\partial v}{\partial x}\right)\end{aligned} \tag{3}$$

which describes strain-rate distribution and strain paths when integrated over time.

As our primary objective is to examine cooling age patterns as a function of footwall velocity and strain fields, our model tracks the time that particles pass through temperatures of 325 °C and 425 °C, corresponding to the ^{40}Ar closure temperatures of biotite and muscovite respectively (Harrison et al., 1985, 2009; Grove and Harrison, 1996; McDougall and Harrison, 1999; Reiners and Brandon, 2006). We use the upper end of the cited closure temperatures as the cooling rate of the tracked particles through the respective closure temperatures is ≥75 °C/Ma in all but the slowest fault slip rates modeled (and generally >100 °C/Ma). The resulting cooling ages for each particle are plotted against the final distance from the fault surface in order to explore cooling age patterns across detachment fault footwalls. All model runs result in 30 km of exhumation of the footwall along the fault surface (~5–25 Ma depending on designated fault slip rate). None of the models achieve thermal steady state over the time scales investigated here, although the rate of isotherm evolution decreases substantially with time during all model runs.

Another primary objective of our study is to examine the effect of footwall erosion during extension on cooling age patterns of higher temperature thermochronometers during detachment faulting. In our models no particles are allowed to move above the surface (y = 0) (i.e. build topography). Thus, particles reaching the surface are treated as being removed immediately (i.e. eroded away).

2.2. Forward modeling of the effects of footwall deformation style

To test differences in cooling age patterns from various footwall strain paths, the thermal evolution of five different velocity fields was determined (Fig. 1). The velocity fields used to test the thermal effects of the following detachment fault kinematic scenarios are: (1) rigid translation and exhumation of a footwall (Fig. 1A), (2) exhumation through a flexural rolling hinge with no footwall erosion (i.e. Buck, 1988) (Fig. 1B), (3) exhumation through a vertical simple shear rolling hinge with no footwall erosion (i.e., Wernicke and Axen, 1988) (Fig. 1C), (4) exhumation through a flexural rolling hinge with erosion of footwall material (Fig. 1D), and (5) exhumation through a vertical, simple shear rolling hinge with erosion of footwall material (Fig. 1E). In all of the numerical simulations, we use a fault dip of 45° and fault slip rates of 2 mm/yr, 6 mm/yr, and 10 mm/yr respectively. As there is no development of topography in the model, slip rate and exhumation rate are directly related. The fault slip rate is referred to in individual velocity field models.

2.2.1. Rigid footwall

For translation of a completely rigid footwall along a fault with a constant dip angle of θ and a slip velocity U on the fault, every

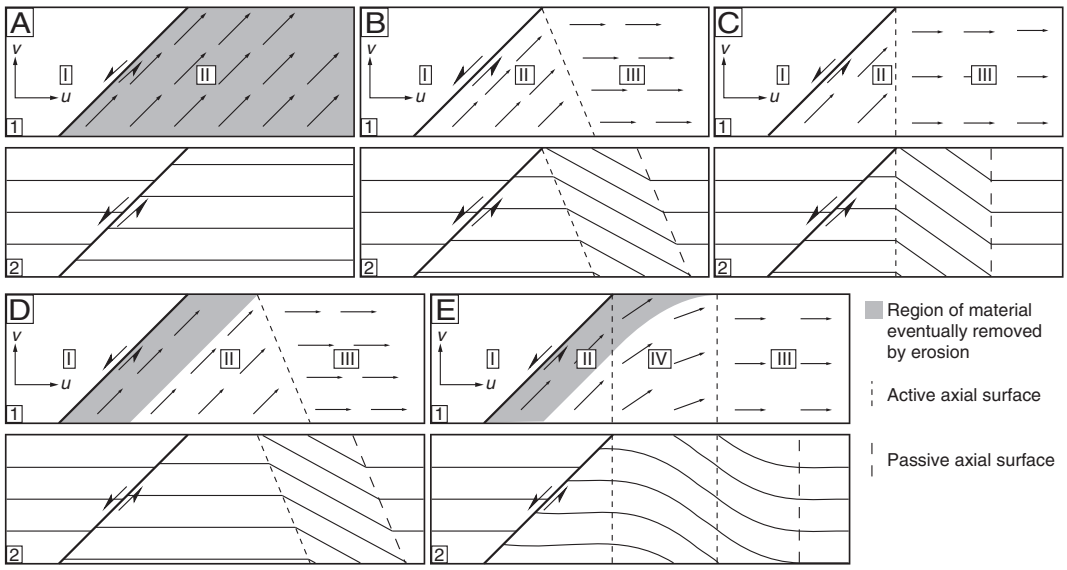

Fig. 1. Diagrams showing the velocity field (1) and originally horizontal displaced footwall material lines (2) for different kinematic models: (A) rigid footwall, (B) flexural rolling hinge, (C) sub-vertical simple shear rolling hinge, (D) flexural rolling hinge with erosion, and (E) sub-vertical simple shear rolling hinge with erosion. Gray areas in (1) for A, D, and E show footwall regions which are 'eroded' after reaching the surface.

point in the footwall has the same velocity as the slip velocity on the fault:

$$\begin{aligned} \overrightarrow{U} &= (u, v) \\ u &= |U|\cos\theta \\ v &= |U|\sin\theta \end{aligned} \tag{4}$$

where u and v are the horizontal and vertical velocity components (region II, Fig. 1A). This results in all particles in the footwall being subject to erosion and all footwall particles exposed at the surface at a given time originating from the same depth. Although this is an oversimplified situation, it allows us to evaluate the thermal evolution of particles originally located at varying horizontal distances from the fault surface. The most important observation is that *P–T* paths of particles exposed at the surface become progressively more concave and *T–t* paths get progressively more convex farther from the fault surface (Fig. 2A and B). At a position ~20 km from the fault, exhumed particles experience near isothermal decompression. This is followed

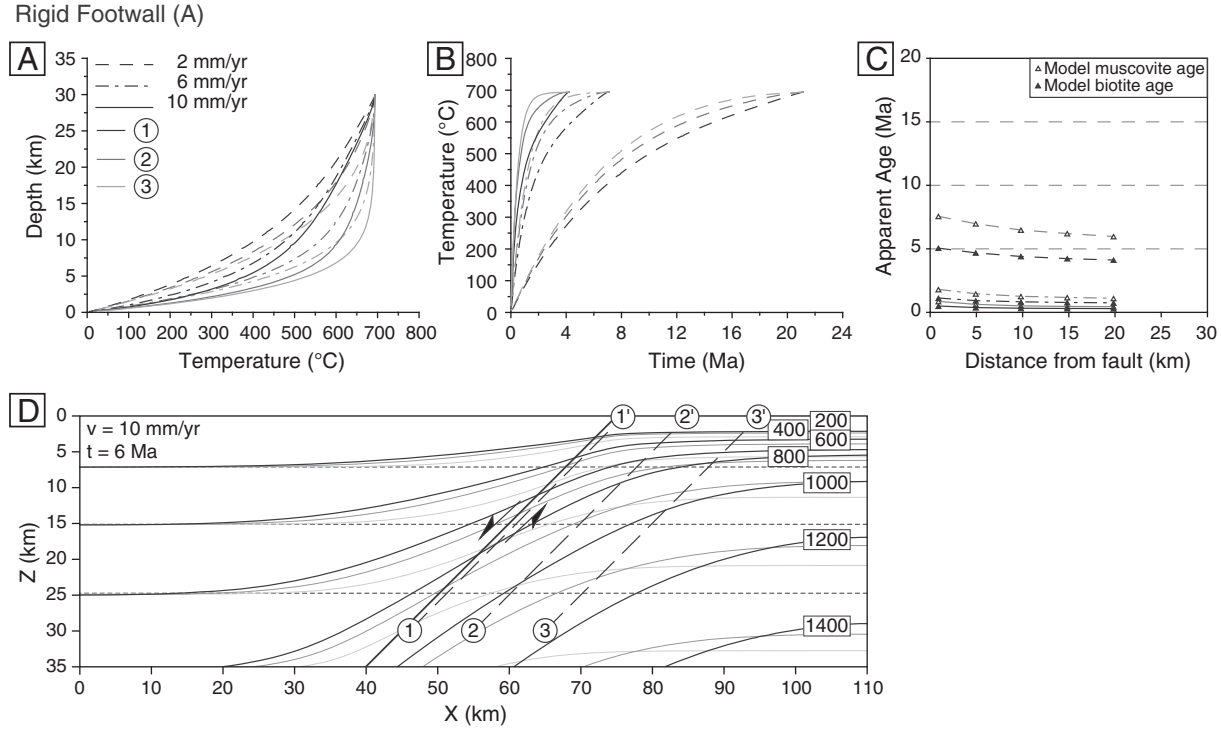

Fig. 2. Rigid-footwall model. (A) Pressure–temperature, and (B) temperature–time curves for samples exhumed in a rigidly uplifted and eroded normal fault footwall. Different line patterns represent P–T and T–t curves for different slip rates. Line shades represent the three particles tracked during exhumation. (C) Modeled patterns of the change in cooling age with distance from the fault. (D) Modeled evolution of isotherms from initially horizontal isotherms (dotted line) in three equally spaced time slices during the kinematic model (progressively darker solid lines). The isotherm diagram also shows the location of the fault (heavy solid lines), the location of changes in the velocity field (thin solid lines), and the particles tracked for the P–T and T–t curves and their strain path (numbers and dashed lines).

by rapid cooling (i.e. hundreds of °C/Ma) in the final stages of exhumation under moderate (6 mm/yr) to rapid (10 mm/yr) slip rates. In this simple model, the lateral variation in cooling histories produces an interesting age pattern: footwall cooling ages decrease with distance from the fault (Fig. 2C). This pattern is opposite to what is generally observed across detachment fault footwalls where cooling ages increase with distance from the fault.

2.2.2. Flexural rolling hinge

The kinematics of a detachment footwall passing through a flexural rolling hinge (i.e. Buck, 1988) was modeled by rotating particle paths across a kink-band fold axis located at the surface intersection of the fault (Figs. 1B and 3). Material below the fold axis has the same velocity and vector as the fault (Fig. 1B, region II), similar to the rigid-footwall case discussed above with the following velocity distribution

$$\begin{aligned}\vec{U} &= (u, v)\\ u &= |U|\cos\theta\\ v &= |U|\sin\theta\end{aligned} \tag{5}$$

where U is the fault slip velocity. Above the fold axis (Fig. 1B, region III), the footwall is transported horizontally parallel to the ground surface at the same rate (U), expressed as

$$\begin{aligned}\vec{U} &= (u, v)\\ u &= |U|\\ v &= 0\end{aligned} \tag{6}$$

The kinematic model requires all footwall particles exposed at the surface during exhumation to have started immediately below the fault surface, being brought to the surface along the same strain path directly beneath the fault but from different depths (i.e. particles 1 and 3 in Fig. 3).

While T–t paths are concave, reflecting the evolving isotherms during exhumation, none of the samples experience the isothermal decompression and subsequent drastic increase in cooling rate observed in the rigid-footwall model. Cooling age patterns show a nearly linear increase in age with distance from the fault (Fig. 3C), reproducing documented cooling age patterns observed in the footwalls of many detachment faults. (e.g. John and Foster, 1993; Foster and John, 1999; Brady, 2002; Carter et al., 2004; Brichau et al., 2008).

2.2.3. Vertical simple shear rolling hinge

In order to investigate possible differences in the evolution of the footwall thermal structure and cooling age patterns between end-member rolling hinge models we examined the thermal effect of a vertical simple shear rolling hinge model (Wernicke and Axen, 1988; Axen and Bartley, 1997). In the model all footwall particles have the same horizontal velocity, while the vertical velocity component was confined to the portion of the footwall directly below the fault (Figs. 1C and 4) such that for region II the velocity field is:

$$\begin{aligned}\vec{U} &= (u, v)\\ u &= |U|\cos\theta\\ v &= |U|\sin\theta\end{aligned} \tag{7}$$

and for region III the velocity field is:

$$\begin{aligned}\vec{U} &= (u, v)\\ u &= |U|\cos\theta\\ v &= 0.\end{aligned} \tag{8}$$

This results in a decrease in absolute velocity as material moves from region II to region III.

Thermal histories of exhumed footwall particles in the vertical simple shear hinge zone are nearly identical to those in a flexural rolling hinge zone for the same slip rate and fault dip angle (Fig. 4A and B). Isotherms are also similar, although; (1) isotherm peaks are roughly vertical, aligned directly below the surface intersection of the fault while isotherm peaks dip steeply away from the hanging wall in the flexural hinge model, and (2) isotherm peaks are slightly higher in the flexural hinge model. Footwall cooling age patterns are telescoped

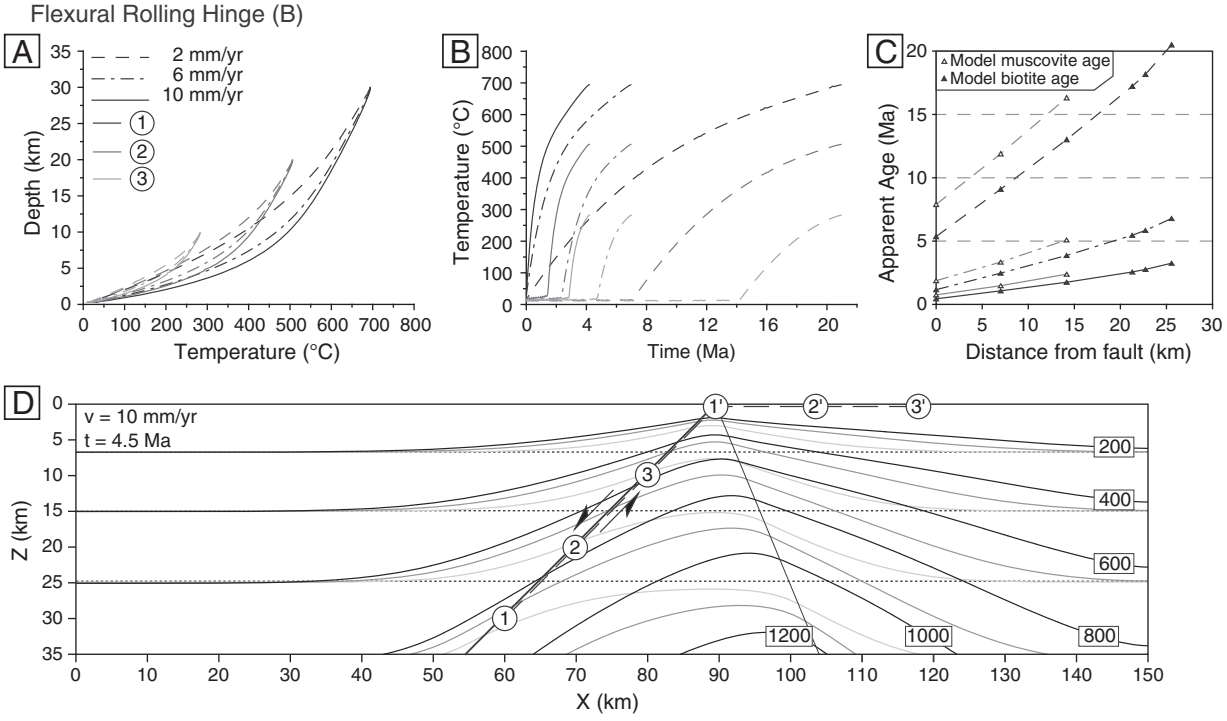

Fig. 3. Flexural rolling hinge model. Details the same as Fig. 2.

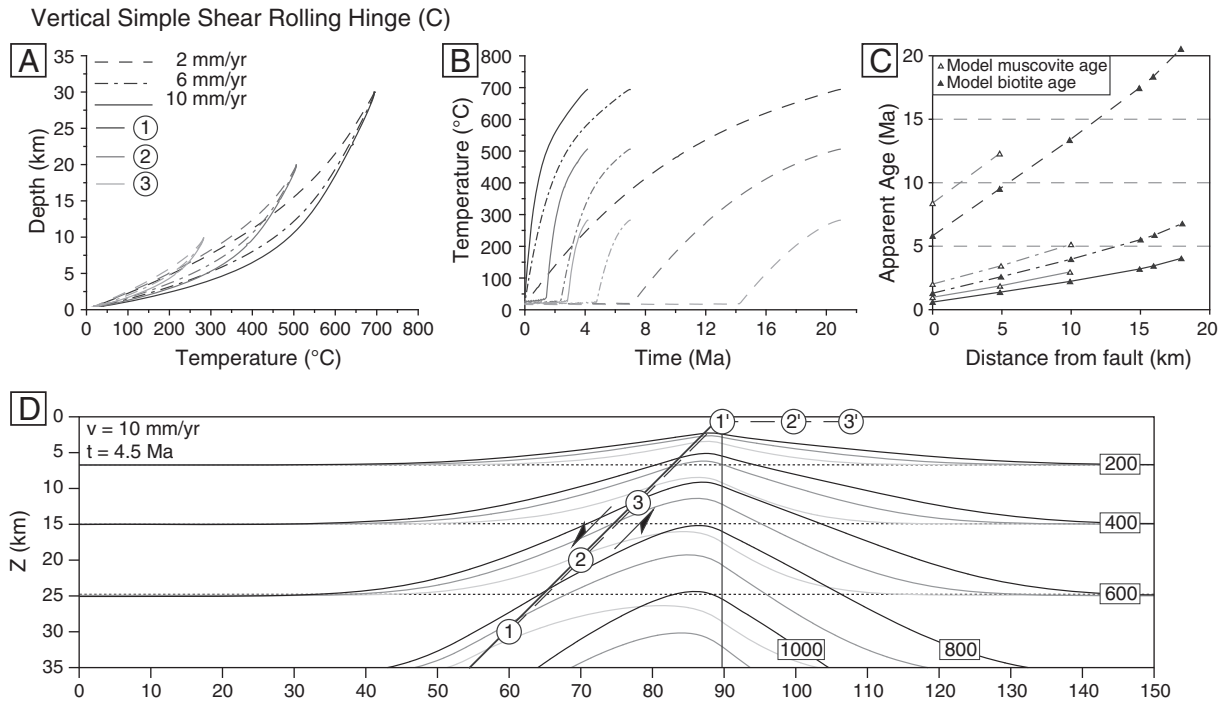

Fig. 4. Vertical simple shear rolling hinge model. Details the same as Fig. 2.

relative to the flexural hinge model as particles in region II have a higher absolute velocity than those in region III. This results in decreasing the distance between exhumed particles as they pass through the hinge. The degree of telescoping scales with the fault dip angle as *cos θ* such that the effect is more pronounced for steeper dipping faults and leads to underestimating the fault slip rate.

2.2.4. Flexural rolling hinge with erosion

In order to simulate erosion of footwall material during exhumation coupled with a flexural rolling hinge, the axis of the hinge zone of the footwall was moved away from the tip of the fault such that the zone of footwall material between the fault and hinge axis is removed (i.e. 'eroded') once it reaches the surface as in the rigid-footwall case (Figs. 1D and 5). This velocity field results in all particles at the surface between the fault and the hinge having been exhumed from the same depth, while behind the hinge all particles are exhumed along the same strain path but from different depths. The effect on the footwall cooling age pattern is a hybrid of the cooling age patterns for rigid-footwall uplift and exhumation with a flexural rolling hinge (Fig. 5C). Ages between the hinge and the hanging wall decrease slightly with distance from the fault, while ages behind the hinge increase with distance from the fault.

2.2.5. Vertical simple shear rolling hinge with erosion

In order to simulate uplift and erosion of the footwall during extension for the vertical simple shear model, a vertical component of the velocity field was maintained in the footwall after the material passed horizontally beyond the tip of the fault, linearly decreasing to zero over a specified distance from the fault, d_1 (Figs. 1E, 6, and 7). The velocity field is therefore defined by three regions (Fig. 1E), with fields II and III the same as fields II and III from the vertical simple shear model (Fig. 1C). Field IV in this model has a velocity field:

$$\begin{aligned} \vec{U} &= (u, v) \\ u &= |U|\cos\theta \\ v &= \frac{d_1 - d_2}{d_1}|U|\sin\theta \end{aligned} \quad [9]$$

where d_1 is the horizontal distance from the fault tip to the point where the vertical velocity component reaches 0, and *d2* is the horizontal distance from the fault tip to a given point in region III. Thus, like the vertical simple shear model, the total velocity decreases across region IV between regions II and III as the horizontal velocity remains constant as the vertical velocity goes to 0.

Exploring the role of erosion of the footwall under this strain regime has a significant advantage over the flexural rolling hinge with coupled erosion (FRE) model as it produces a more realistic pattern of predicted footwall pressures after exhumation. In the FRE model predicted footwall pressures are constant between the hinge and the fault tip. In this model however, predicted footwall pressures steadily decrease away from the fault across the entire footwall.

Footwall cooling age patterns of a vertical simple shear hinge with erosion are convex (Fig. 6C), with an increasing age gradient with distance from the fault. Faster slip rates decrease the convexity of the age gradient, and increasing the width of the region over which erosion occurs (d_1) increases the convexity (Fig. 7). These results are similar to modeled footwall age patterns of low-temperature thermochronometers in high-angle normal faults which incorporate footwall erosion (e.g. Ehlers et al., 2003). Unlike the cooling patterns from flexural rolling hinge with erosion there is no sharp inflection point in ages with distance from the fault.

3. Discussion and summary of forward modeling results

3.1. Discussion of model parameters

Detachment fault hanging walls exhibit a wide variety of behavior, from those that are extensively deformed during extension (broken upper-plate model of Yin, 2004) to those that show little or no deformation during extension (unbroken upper-plate model of Yin, 2004). As the hanging wall in our models is a fixed rigid block, our modeling focuses on the general class of unbroken upper-plate detachment which include a large number of detachment systems (e.g. Pan and Kidd, 1992; Cogan et al., 1998; Murphy et al., 2002; Robinson et al., 2004; Kapp et al., 2005; Giovanni et al., in press). However, it is important to note that even in detachment systems

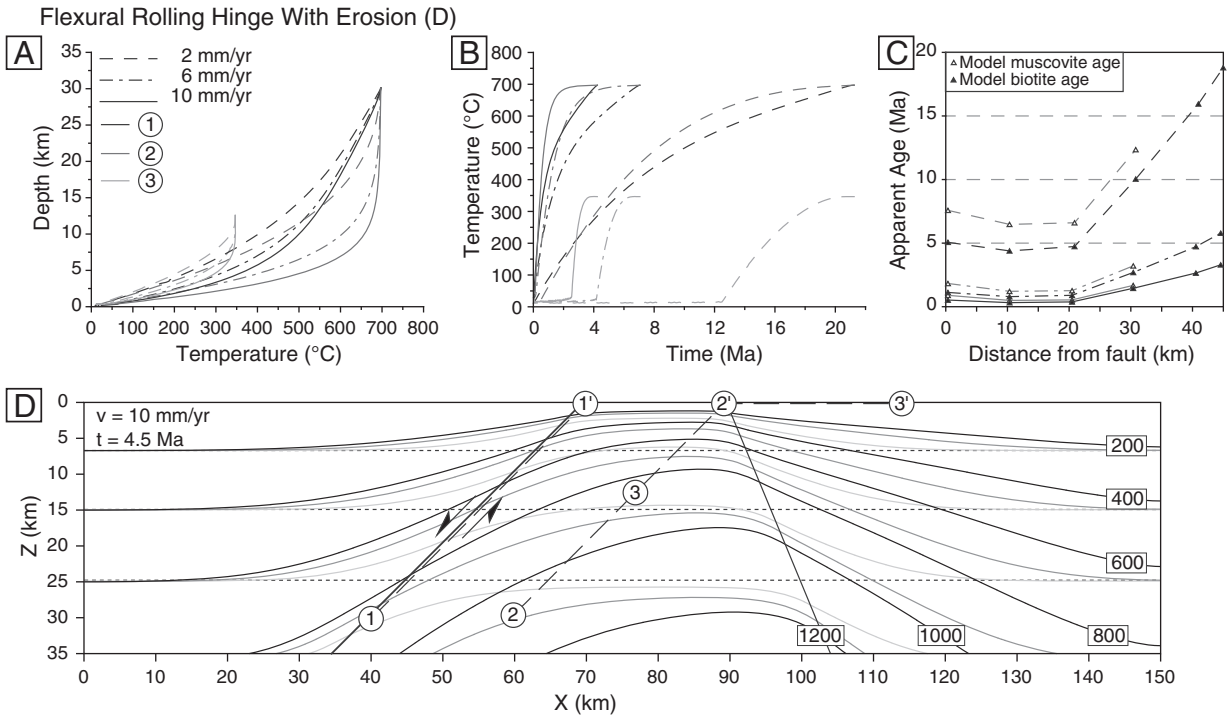

Fig. 5. Flexural rolling hinge with erosion model. Details the same as Fig. 2.

where hanging walls are cut by numerous normal faults (broken upper-plate model), the total magnitude of extension is generally much smaller than the amount of slip on the detachment fault. Thus, the use of a broken upper-plate model would not likely have a significant impact on our results. Another aspect of our hanging wall parameterization is that hanging wall subsidence and basin formation are not taken into account. This is a reasonable simplification as basins in detachment fault settings are generally thin (1–3 km) to absent, (e.g. Friedmann and Burbank, 1995). Thus, hanging wall subsidence and basin formation are not significant factors in the thermal evolution of most extensional detachment fault systems.

During the evolution of our models, we also do not include any advection of material across the fault, either from the hanging wall to the footwall or vice versa. While some detachment fault systems show evidence of transfer of material from the hanging wall to the footwall (i.e. excisment of Davis and Lister, 1988), the amount of material

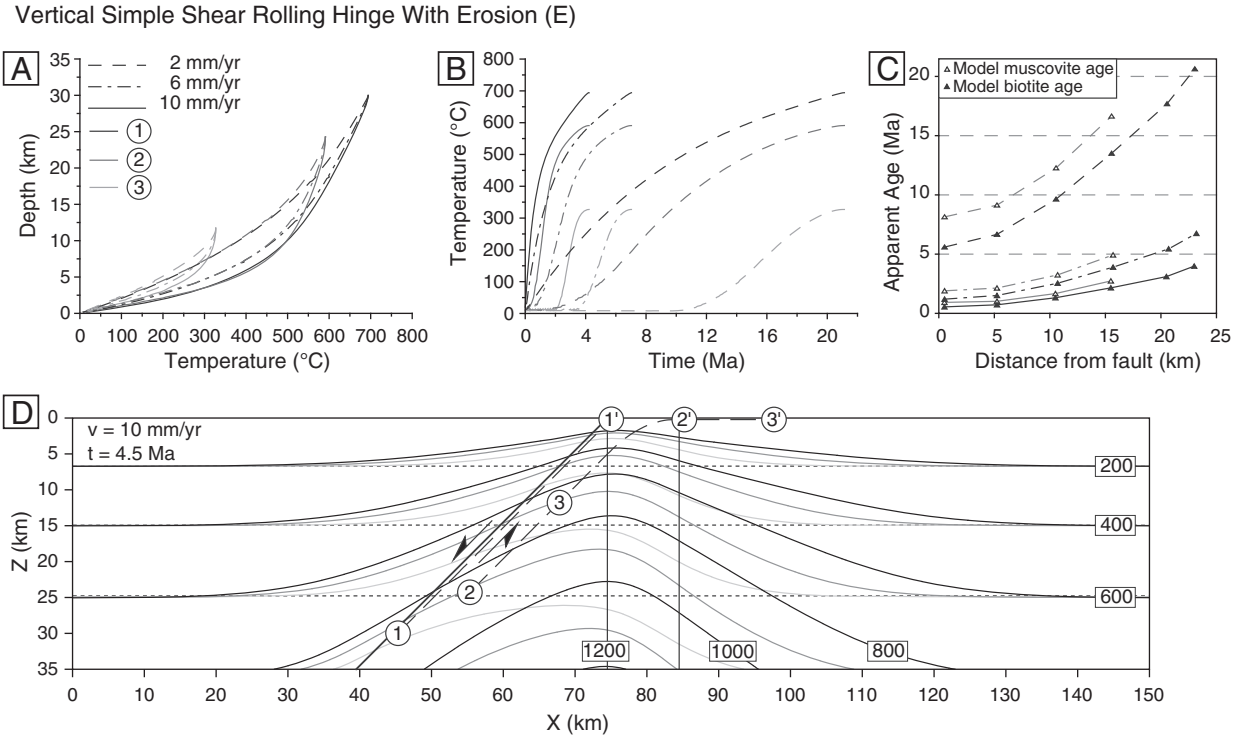

Fig. 6. Vertical simple shear rolling hinge with erosion model. Details the same as Fig. 2.

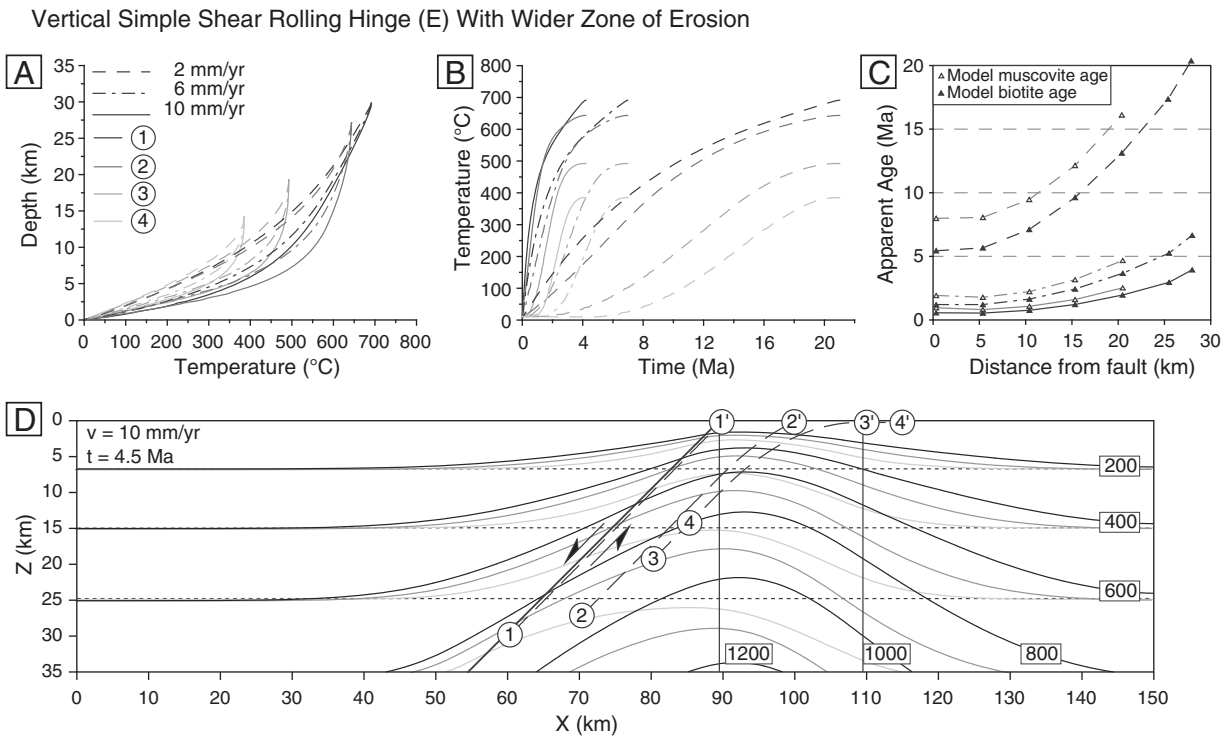

Fig. 7. Vertical simple shear rolling hinge with erosion with a wider zone of erosion (D).

transferred is generally relatively thin (several hundred meters at most, e.g., Lister and Davis, 1989; Murphy et al., 2002), and would not significantly affect the thermal structure of the system or the results from this study.

Another aspect of our model is the lack of topography development during extension. While detachment faulting can certainly create topography, the amount of topography that develops in most extensional systems (several km at most) is not enough to significantly effect the position of isotherms for the higher temperature thermochronometers being evaluated in this study (e.g. Mancktelow and Grasemann, 1997; Braun, 2002), and would have minimal impact on the modeled cooling age patterns. Additionally, while dynamic feedback between fault slip rates, topography, and enhanced erosion has been proposed, the mechanism appears to apply only to rather special tectonic settings under specific climatic conditions (e.g. Zeitler et al., 2001). For example, the proposed positive feedback for the development of the Himalayan orogen by Beaumont et al. (2001) is not supported by thermochronologic work in Nepal (Burbank et al., 2003) and the structural work of Yin (2006) and Webb et al. (2007). As this is an important but still unsettled problem, we leave the modeling efforts on potential feedback among fault motion, extension-induced topography and topographic enhanced erosion that may lead to fault slip variations to later studies.

In regards to fault dip angle, we found that the simulated footwall thermal histories are rather insensitive to fault dip angle as long as the vertical exhumation rate is the same. A fault dip of 20° with the same vertical exhumation rate (v) as a fault dip of 45° yields essentially the same thermal history. This conclusion is similar to that reached by Ruppel et al. (1988). For this reason we restricted our general modeling to faults with a 45° dip angle.

3.2. Forward modeling results and implications

Effects on our modeled muscovite and biotite cooling age patterns come from two different processes: (1) advection of isotherms from exhumation of footwall material during slip on the fault, and (2) the non-uniform advection of isotherms which results in different footwall particle strain paths passing through different evolving thermal gradients.

In our models where all exhumed footwall particles follow the same strain path and the latter can be ignored (i.e. the flexural and vertical simple shear rolling hinges without erosion), cooling age patterns show a nearly linear increase in age with distance from the fault (Figs. 3C and 4C). The linear relationship of age vs. distance reproduces observed cooling age patterns in the footwalls of many detachment faults. These relationships are often used to calculate fault slip rates in detachment fault systems based on the assumption that the isotherm for a given thermochronometer is static during exhumation (e.g. John and Foster, 1993; Foster and John, 1999; Wells et al., 2000; Brady, 2002; Carter et al., 2004, 2006; Brichau et al., 2008). However, as noted by Ketcham (1996), isotherms continue to evolve during slip, especially for the higher temperature isotherms at high slip rates (e.g. Figs. 3D and 4D), and failure to take into account isotherm advection leads to underestimating the actual slip rate. As an example, the muscovite age distribution for a slip rate of 10 mm/yr from Fig. 3C yields a calculated slip rate of 7.3 mm/yr if one assumes static isotherms, 28% less than the actual slip rate. For the vertical simple shear model, where rates from the cooling age trend are equivalent to the extension rate across the fault (u) rather than the fault sip rate, the calculated extension rate suffers the same error that results from the non-static nature of the isotherms discussed above.

The non-uniform advection of isotherms in our evolving models is a result of two processes; (1) conductive cooling from the hanging wall which results in slower isotherm advection adjacent to the fault, and (2) relaxation of the advected footwall isotherms where there is no longer a vertical velocity component. These effects were noted in earlier studies which focused on tracking the thermal history of particles along the fault surface (Ruppel et al., 1988; Ketcham, 1996), although the effects on cooling age patterns were not explored.

In our model where a completely rigid footwall is exhumed uniformly, the latter of these effects is not present. This results in particles further from the fault passing though higher thermal gradients, and cooling later in the exhumation history which results in footwall ages decreasing with distance from the fault, opposite to what is

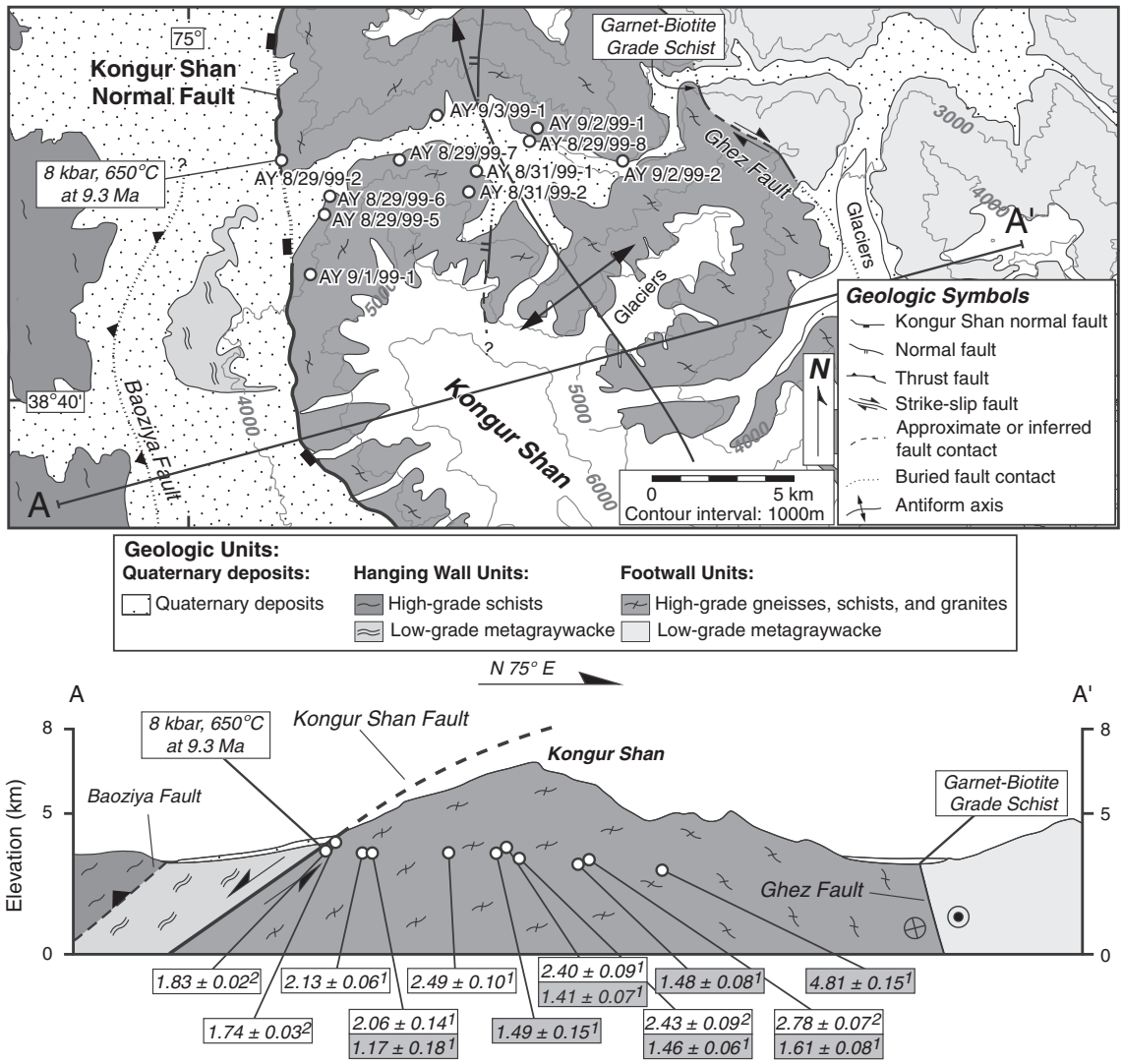

Fig. 9. Simplified geologic map (A) and cross section (B) of the Kongur Shan massif showing cooling age sample localities and the sample locality used for pre-extension P–T–t analyses (Robinson et al., 2004). The cross section shows the sample localities and the muscovite (white) and biotite (gray) ages from each sample with their relative distance from the fault and elevation projected onto the cross section. ([1]this study; [2]Robinson et al., 2004.

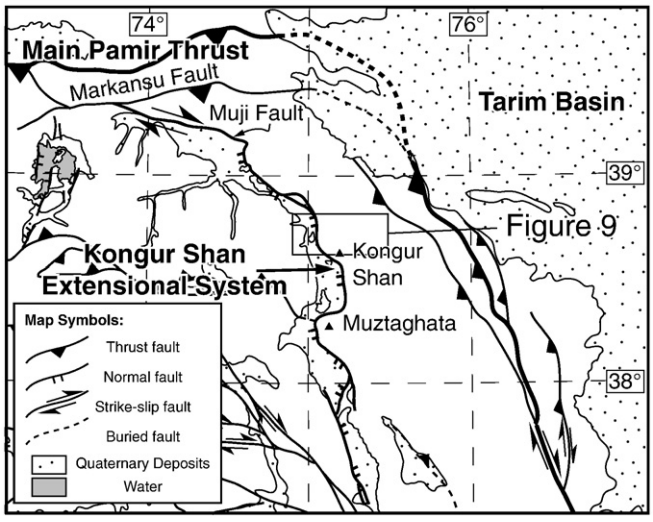

Fig. 8. Simplified tectonic map of the eastern Pamir.

generally observed. While this model is an oversimplification, it illustrates that in deeply eroded detachment fault footwalls samples collected at different distances from the fault will have passed through different evolving thermal gradients. This will complicate the interpretation of cooling age patterns.

The most striking aspect of our exploration of the variation in cooling age patterns from the flexural and vertical simple shear rolling hinge models which incorporate footwall erosion during extension is the strongly non-linear increase in age with distance from the fault (Figs. 5C, 6C, and 7C). This non-linear increase in cooling age with distance has important implications for interpreting thermochronologic data from detachment fault footwalls that have experienced significant (i.e. several km) erosion: (1) The slope of the change in age with distance from the fault cannot be used to calculate the slip rate/extension rate of the fault, as is often used in detachment fault settings, and (2) Changes in the slope of age vs. distance from fault do not represent changes in the slip rate/extension rate. These results demonstrate that erosion of footwall material during exhumation can significantly affect cooling age patterns in extensional systems for higher temperature thermochronometers (e.g., Moore and England, 2001) as has been demonstrated for lower temperature systems (e.g., Ehlers et al., 2001). These results also highlight the complexities in

Table 2
Ar isotopic data from muscovite and biotite step-heating analyses.

AY8-29-99-5	Muscovite	6.8 mg	J = 0.003562							Location: 38°43′28.45″N, 75° 3′4.80″E		
T (C)	t (min)	$^{40}Ar/^{39}Ar$	$^{38}Ar/^{39}Ar$	$^{37}Ar/^{39}Ar$	$^{36}Ar/^{39}Ar$	^{39}Ar (mol)	$\Sigma^{39}Ar$	$\%^{40}Ar^*$	$^{40}Ar^*/^{39}Ar_K$	$\pm\sigma_{40/39}$	Age (Ma)	$\pm\sigma_{Age}$
500	13	81.75402	2.43E−01	2.48E−02	2.74E−01	2.56E−15	0.3767822	1.003215	0.8221373	1.21E+00	5.28	7.75
600	13	7.814464	2.31E−02	2.48E−02	2.47E−02	5.80E−15	1.23142	5.963266	0.4711253	2.75E−01	3.02	1.76
700	13	3.048504	1.79E−02	2.48E−02	9.43E−03	1.98E−14	4.147054	7.498489	0.2304833	9.42E−02	1.48	0.61
770	13	2.154924	1.51E−02	2.48E−02	6.29E−03	3.43E−14	9.205058	12.19741	0.2646195	5.43E−02	1.70	0.35
840	13	1.165158	1.41E−02	2.48E−02	2.64E−03	1.05E−13	24.72491	30.2389	0.3537675	1.86E−02	2.27	0.12
880	13	0.6903958	1.37E−02	2.48E−02	1.08E−03	1.16E−13	41.78046	49.14037	0.3413835	1.52E−02	2.19	0.10
920	13	0.7275982	1.39E−02	2.48E−02	1.30E−03	7.59E−14	52.96482	42.46552	0.3117701	1.96E−02	2.00	0.13
960	13	0.7857587	1.38E−02	2.48E−02	1.49E−03	6.68E−14	62.80926	39.82101	0.3158709	2.10E−02	2.03	0.13
1000	13	0.7218317	1.39E−02	2.48E−02	1.26E−03	7.56E−14	73.94882	43.81194	0.3191403	2.02E−02	2.05	0.13
1070	13	0.5284899	1.35E−02	2.48E−02	5.46E−04	1.58E−13	97.22461	63.24535	0.3362454	9.81E−03	2.16	0.06
1150	13	0.9181083	1.47E−02	2.48E−02	2.05E−03	1.56E−14	99.53058	29.76892	0.2827874	7.91E−02	1.82	0.51
1350	13	3.862625	1.94E−02	2.48E−02	1.08E−02	3.18E−−15	99.99	16.05223	0.6451371	4.39E−01	4.14	2.82
AY8/29/99-6	Muscovite	6.8 mg	J = 0.003564							Location: 38°43′49.13″N, 75° 3′13.47″E		
T (C)	t (min)	$^{40}Ar/^{39}Ar$	$^{38}Ar/^{39}Ar$	$^{37}Ar/^{39}Ar$	$^{36}Ar/^{39}Ar$	^{39}Ar (mol)	$\Sigma^{39}Ar$	$\%^{40}Ar^*$	$^{40}Ar^*/^{39}Ar_K$	$\pm\sigma_{40/39}$	Age (Ma)	$\pm\sigma_{Age}$
500	13	74.56068	1.55E−01	4.95E−02	2.45E−01	5.04E−15	0.8761009	2.768299	2.06664	1.80E+00	13.2	11.5
600	13	12.57005	4.29E−02	4.95E−02	4.12E−02	3.79E−15	1.534759	2.846677	0.3612643	5.37E−01	2.32	3.45
700	13	3.462857	2.20E−02	4.95E−02	1.09E−02	1.32E−14	3.822846	6.408617	0.2241477	1.22E−01	1.44	0.78
770	13	2.88074	1.61E−02	4.95E−02	8.83E−03	2.41E−14	8.005869	8.393751	0.2434006	7.52E−02	1.56	0.48
840	13	1.471148	1.36E−02	4.95E−02	3.55E−03	1.37E−13	31.81115	26.75456	0.3945045	1.77E−02	2.53	0.11
880	13	0.7474509	1.33E−02	4.95E−02	1.35E−03	1.02E−13	49.54972	42.4349	0.3190865	1.83E−02	2.05	0.12
920	13	0.8891822	1.35E−02	4.95E−02	1.93E−03	5.90E−14	59.80279	32.46544	0.2911952	2.63E−02	1.87	0.17
960	13	1.152467	1.40E−02	4.95E−02	2.71E−03	3.78E−14	66.36668	27.77498	0.32346	3.90E−02	2.08	0.25
1000	13	1.370041	1.42E−02	4.95E−02	3.60E−03	2.90E−14	71.40684	20.13003	0.2789626	5.08E−02	1.79	0.33
1070	13	1.121755	1.38E−02	4.95E−02	2.61E−03	5.08E−14	80.24377	28.4392	0.3215786	3.28E−02	2.07	0.21
1150	13	0.7445859	1.32E−02	4.95E−02	1.29E−03	8.89E−14	95.70293	44.52171	0.3337955	2.24E−02	2.14	0.14
1350	13	2.439988	2.18E−02	4.95E−02	3.46E−03	2.47E−14	99.99	56.52688	1.389714	5.67E−02	8.91	0.36
AY8/29/99-6	Biotite	6.8 mg	J = 0.003565							Location: 38°43′49.13″N, 75° 3′13.47″E		
T (C)	t (min)	$^{40}Ar/^{39}Ar$	$^{38}Ar/^{39}Ar$	$^{37}Ar/^{39}Ar$	$^{36}Ar/^{39}Ar$	^{39}Ar (mol)	$\Sigma^{39}Ar$	$\%^{40}Ar^*$	$^{40}Ar^*/^{39}Ar_K$	$\pm\sigma_{40/39}$	Age (Ma)	$\pm\sigma_{Age}$
500	13	36.78879	1.90E−01	4.95E−02	1.25E−01	1.90E−14	4.565648	−0.08922618	−0.0328546	7.18E−01	0.00	0.00
600	13	13.28534	1.47E−01	4.95E−02	4.44E−02	4.81E−14	16.11281	1.099853	0.1462688	1.19E−01	0.94	0.77
700	13	8.264533	1.43E−01	4.95E−02	2.74E−02	9.47E−14	38.86028	1.715766	0.1419197	6.55E−02	0.91	0.42
770	13	6.868504	1.43E−01	4.95E−02	2.27E−02	5.58E−14	52.26083	2.005423	0.1379735	7.02E−02	0.89	0.45
840	13	6.90312	1.51E−01	4.95E−02	2.26E−02	2.22E−14	57.58533	2.661601	0.1844923	1.17E−01	1.19	0.75
900	13	6.058417	1.46E−01	4.95E−02	1.97E−02	3.53E−14	66.06875	3.553523	0.2159255	8.15E−02	1.39	0.52
960	13	5.692569	1.48E−01	4.95E−02	1.84E−02	5.57E−14	79.43336	3.797003	0.2165828	6.36E−02	1.39	0.41
1050	13	5.617729	1.44E−01	4.95E−02	1.82E−02	7.22E−14	96.7813	3.611961	0.2032315	5.68E−02	1.31	0.36
1150	13	5.27384	1.10E−01	4.95E−02	1.66E−02	8.88E−15	98.91257	6.57659	0.3514882	2.00E−01	2.26	1.28
1350	13	10.85898	6.42E−02	4.95E−02	2.80E−02	4.53E−15	99.99	23.1314	2.54388	3.94E−01	16.3	2.5
AY8/29/99−7	Muscovite	6.8 mg	J = 0.003572							Location: 38°44′42.38″N, 75° 4′54.44″E		
T (C)	t (min)	$^{40}Ar/^{39}Ar$	$^{38}Ar/^{39}Ar$	$^{37}Ar/^{39}Ar$	$^{36}Ar/^{39}Ar$	^{39}Ar (mol)	$\Sigma^{39}Ar$	$\%^{40}Ar^*$	$^{40}Ar^*/^{39}Ar_K$	$\pm\sigma_{40/39}$	Age (Ma)	$\pm\sigma_{Age}$
500	13	69.14487	1.53E−01	4.95E−02	2.39E−01	4.84E−15	0.7334159	−2.102781	−1.456629	5.44E+00	0.00	0.00
600	13	11.8582	6.31E−02	4.95E−02	3.93E−02	3.52E−15	1.267078	1.793016	0.2156893	5.98E−01	1.39	3.85
700	13	3.512595	3.15E−02	4.95E−02	1.06E−02	9.83E−15	2.756353	10.01348	0.3578756	1.20E−01	2.30	0.77
770	13	2.120724	2.07E−02	4.95E−02	5.97E−03	1.74E−14	5.393214	15.2181	0.3280047	1.03E−01	2.11	0.66
840	13	1.924904	1.67E−02	4.95E−02	5.19E−03	4.28E−14	11.87277	18.6415	0.3614662	4.61E−02	2.33	0.30
880	13	1.204791	1.57E−02	4.95E−02	2.73E−03	7.33E−14	22.9845	30.49199	0.3698794	2.64E−02	2.38	0.17
920	13	0.897841	1.55E−02	4.95E−02	1.69E−03	1.06E−13	39.10007	40.98231	0.3702874	1.92E−02	2.38	0.12
960	13	0.8799416	1.58E−02	4.95E−02	1.65E−03	1.14E−13	56.417	41.20422	0.3647552	1.66E−02	2.35	0.11

1000	13	0.8910806	1.57E−02	4.95E−02	1.62E−03	9.87E−14	71.37891	42.85363	0.3844848	1.88E−02	2.48	0.12
1070	13	0.742333	1.53E−02	4.95E−02	1.10E−03	1.36E−13	92.04005	51.96156	0.3880342	1.50E−02	2.50	0.10
1150	13	0.9883545	1.57E−02	4.95E−02	1.89E−03	4.11E−14	98.26678	39.99623	0.401172	4.43E−02	2.58	0.29
1350	13	3.431809	2.17E−02	4.95E−02	6.91E−03	1.14E−14	99.99	39.05803	1.360977	1.51E−01	8.75	0.97
AY8-29-99-8A	Biotite	6 mg	J = 0.003574							Location: 38°44′59.94″N, 75° 8′17.41″E		
T (C)	t (min)	$^{40}Ar/^{39}Ar$	$^{38}Ar/^{39}Ar$	$^{37}Ar/^{39}Ar$	$^{36}Ar/^{39}Ar$	^{39}Ar (mol)	$\Sigma^{39}Ar$	$\%^{40}Ar^*$	$^{40}Ar^*/^{39}Ar_K$	$\pm\sigma_{40/39}$	Age (Ma)	$\pm\sigma_{Age}$
500	13	133.456	1.29E−01	2.48E−02	4.49E−01	3.90E−15	0.6880271	0.4586063	0.6126927	9.97E + 00	3.95	64.13
600	13	14.04268	2.35E−02	2.48E−02	4.56E−02	1.64E−14	3.586748	3.768872	0.5305156	3.09E−01	3.42	1.99
700	13	2.961748	1.55E−02	2.48E−02	9.00E−03	8.13E−14	17.92188	9.122311	0.2707994	4.60E−02	1.75	0.30
770	13	1.361357	1.44E−02	2.48E−02	3.60E−03	9.32E−14	34.35553	19.44423	0.2658525	3.78E−02	1.71	0.24
840	13	1.183647	1.43E−02	2.48E−02	3.05E−03	3.76E−14	40.98642	20.8944	0.2503616	4.16E−02	1.61	0.27
900	13	0.9051294	1.41E−02	2.48E−02	2.09E−03	3.17E−14	46.57327	27.87524	0.2571267	4.48E−02	1.66	0.29
960	13	0.7569101	1.38E−02	2.48E−02	1.68E−03	4.96E−14	55.31962	30.03532	0.2306587	3.29E−02	1.49	0.21
1050	13	0.5521333	1.40E−02	2.48E−02	9.82E−04	1.51E−13	81.96519	41.60746	0.2312402	1.17E−02	1.49	0.08
1150	13	0.5771284	1.39E−02	2.48E−02	1.03E−03	1.00E−13	99.68446	41.44636	0.2414608	1.94E−02	1.56	0.13
1350	13	16.99578	2.49E−02	2.48E−02	5.66E−02	1.79E−15	99.99	1.379092	0.2386097	2.85E + 00	1.54	18.33
AY8/31/99-1A	Biotite	6.5 mg J	J = 0.003584							Location: 38°44′23.25″N, 75° 6′41.37″E		
T (C)	t (min)	$^{40}Ar/^{39}Ar$	$^{38}Ar/^{39}Ar$	$^{37}Ar/^{39}Ar$	$^{36}Ar/^{39}Ar$	^{39}Ar (mol)	$\Sigma^{39}Ar$	$\%^{40}Ar^*$	$^{40}Ar^*/^{39}Ar_K$	$\pm\sigma_{40/39}$	Age (Ma)	$\pm\sigma_{Age}$
500	13	98.2672	1.66E−01	2.48E−02	3.29E−01	3.90E−15	0.7265258	0.884301	0.8700977	1.23E + 00	5.62	7.90
600	13	12.11211	4.62E−02	2.48E−02	3.95E−02	1.82E−14	4.12767	3.315318	0.4024467	1.86E−01	2.60	1.20
700	13	2.103433	3.94E−02	2.48E−02	6.10E−03	8.66E−14	20.27367	12.76178	0.2691576	3.04E−02	1.74	0.20
770	13	0.7716211	3.85E−02	2.48E−02	1.76E−03	9.98E−14	38.87793	28.45935	0.2209898	1.69E−02	1.43	0.11
840	13	0.776718	3.87E−02	2.48E−02	1.74E−03	5.21E−14	48.59592	29.37432	0.2309008	2.64E−02	1.49	0.17
900	13	0.8259365	3.80E−02	2.48E−02	1.89E−03	3.56E−14	55.22923	28.35989	0.2381156	3.75E−02	1.54	0.24
960	13	0.7664859	3.87E−02	2.48E−02	1.78E−03	4.66E−14	63.91729	26.87312	0.2087873	3.17E−02	1.35	0.20
1050	13	0.60053	3.87E−02	2.48E−02	1.14E−03	1.40E−13	90.03953	38.70728	0.233797	1.10E−02	1.51	0.07
1150	13	0.9205497	3.81E−02	2.48E−02	2.17E−03	4.67E−14	98.74956	26.58591	0.2475088	3.27E−02	1.60	0.21
1350	14	3.721352	3.80E−02	2.48E−02	1.08E−02	6.71E−15	99.99	13.09005	0.496627	1.99E−01	3.21	1.29
AY8/31/99-2	Muscovite	6.7 mg	J = 0.003587							Location: 38°43′59.07″N, 75° 6′18.80″E		
T (C)	t (min)	$^{40}Ar/^{39}Ar$	$^{38}Ar/^{39}Ar$	$^{37}Ar/^{39}Ar$	$^{36}Ar/^{39}Ar$	^{39}Ar (mol)	$\Sigma^{39}Ar$	$\%^{40}Ar^*$	$^{40}Ar^*/^{39}Ar_K$	$\pm\sigma_{40/39}$	Age (Ma)	$\pm\sigma_{Age}$
500	13	90.00184	1.97E−01	4.95E−02	3.15E−01	4.31E−15	0.6741791	−3.454392	−3.113099	6.62E + 00	0.00	0.00
600	13	10.22459	3.25E−02	4.95E−02	3.41E−02	3.91E−15	1.286724	1.247186	0.1291032	4.62E−01	0.84	2.99
700	13	3.394178	1.67E−02	4.95E−02	1.08E−02	1.13E−14	3.058954	4.722199	0.1623517	1.21E−01	1.05	0.78
770	13	2.763805	1.49E−02	4.95E−02	8.42E−03	1.85E−14	5.960141	8.844034	0.2468041	8.82E−02	1.60	0.57
840	13	2.589881	1.39E−02	4.95E−02	7.50E−03	5.33E−14	14.30492	13.28676	0.3453587	4.01E−02	2.23	0.26
880	13	0.9702182	1.27E−02	4.95E−02	1.91E−03	9.83E−14	29.69634	38.72769	0.3777077	1.82E−02	2.44	0.12
920	13	0.7656347	1.27E−02	4.95E−02	1.24E−03	1.11E−13	47.03581	48.18502	0.3710892	1.54E−02	2.40	0.10
960	13	0.8531328	−3.92E−02	4.95E−02	1.64E−03	1.15E−13	64.98517	39.55033	0.3391386	1.02E−02	2.19	0.07
1000	13	0.9348978	1.27E−02	4.95E−02	1.84E−03	9.60E−14	80.00896	38.57534	0.3626439	1.70E−02	2.35	0.11
1070	13	0.8423996	1.27E−02	4.95E−02	1.43E−03	8.04E−14	92.60023	46.03122	0.390615	1.92E−02	2.53	0.12
1150	13	0.8933335	1.29E−02	4.95E−02	1.83E−03	3.70E−14	98.3846	35.75459	0.3242104	3.67E−02	2.10	0.24
1350	13	2.462637	1.94E−02	4.95E−02	5.69E−03	1.03E−14	99.99	29.93944	0.7516897	1.25E−01	4.86	0.81
AY8/31/99-2	Biotite	6.9 mg	J = 0.00359							Location: 38°43′59.07″N, 75° 6′18.80″E		
T (C)	t (min)	$^{40}Ar/^{39}Ar$	$^{38}Ar/^{39}Ar$	$^{37}Ar/^{39}Ar$	$^{36}Ar/^{39}Ar$	^{39}Ar (mol)	$\Sigma^{39}Ar$	$\%^{40}Ar^*$	$^{40}Ar^*/^{39}Ar_K$	$\pm\sigma_{40/39}$	Age (Ma)	$\pm\sigma_{Age}$
500	13	34.07389	1.03E−01	4.95E−02	1.18E−01	4.79E−15	0.836752	−2.501247	−0.8560493	1.24E + 00	0.00	0.00
600	13	11.06293	2.50E−02	4.95E−02	3.66E−02	1.09E−14	2.740346	2.028898	0.225801	2.36E−01	1.46	1.52
700	13	2.716122	1.67E−02	4.95E−02	8.40E−03	5.47E−14	12.29166	7.495027	0.2045664	4.55E−02	1.32	0.29
770	13	0.8095762	1.52E−02	4.95E−02	1.91E−03	1.06E−13	30.77678	26.48288	0.216204	1.17E−02	1.40	0.08
840	13	0.5655621	1.47E−02	4.95E−02	1.13E−03	9.62E−14	47.57135	35.43555	0.2030636	1.84E−02	1.31	0.12
900	13	0.7478008	1.51E−02	4.95E−02	1.65E−03	4.48E−14	55.39655	30.11578	0.23004	3.59E−02	1.49	0.23
960	13	0.8389814	1.52E−02	4.95E−02	2.12E−03	3.91E−14	62.22053	21.33788	0.1829484	3.63E−02	1.18	0.23

(continued on next page)

Table 2 (*continued*)

AY8/31/99-2	Biotite	6.9 mg	J = 0.00359							Location: 38°43′59.07″N, 75° 6′18.80″E		
T (C)	t (min)	$^{40}Ar/^{39}Ar$	$^{38}Ar/^{39}Ar$	$^{37}Ar/^{39}Ar$	$^{36}Ar/^{39}Ar$	^{39}Ar (mol)	$\Sigma^{39}Ar$	$\%^{40}Ar^*$	$^{40}Ar^*/^{39}Ar_K$	$\pm\sigma_{40/39}$	Age (Ma)	$\pm\sigma_{Age}$
1050	13	0.6214049	1.50E−02	4.95E−02	1.27E−03	1.17E−13	82.67921	34.60545	0.2171694	1.47E−02	1.41	0.10
1150	13	0.8382413	1.52E−02	4.95E−02	1.98E−03	7.69E−14	96.09898	26.62915	0.2257134	2.30E−02	1.46	0.15
1350	13	1.688136	1.68E−02	4.95E−02	3.80E−03	2.23E−14	99.99	31.2688	0.5379283	6.36E−02	3.48	0.41
AY9/2/99-1	Biotite	7.4 mg	J = 0.003474303							Location: 38°45′12.08″N, 75° 8′26.35″E		
T (C)	t (min)	$^{40}Ar/^{39}Ar$	$^{38}Ar/^{39}Ar$	$^{37}Ar/^{39}Ar$	$^{36}Ar/^{39}Ar$	^{39}Ar (mol)	$\Sigma^{39}Ar$	$\%^{40}Ar^*$	$^{40}Ar^*/^{39}Ar_K$	$\pm\sigma_{40/39}$	Age (Ma)	$\pm\sigma_{Age}$
500	13	95.00290	1.39E−01	4.95E−02	3.20E−01	4.19E−15	0.6757839	0.3789318	0.3606293	4.50E+00	2.26	28.18
600	0	20.12626	4.15E−02	4.95E−02	6.14E−02	6.76E−15	1.766173	9.60829	1.943587	1.19E−01	12.1	0.7
700	13	7.25332	2.49E−02	4.95E−02	2.29E−02	4.99E−14	9.821986	6.295485	0.4575119	7.75E−02	2.87	0.49
770	13	1.50202	1.89E−02	4.95E−02	4.01E−03	1.08E−13	27.21453	19.20377	0.2896744	3.00E−02	1.81	0.19
840	13	1.11625	1.83E−02	4.95E−02	2.71E−03	6.46E−14	37.63599	25.44743	0.2867643	2.34E−02	1.80	0.15
900	0	1.78034	−3.40E−02	4.95E−02	4.96E−03	3.88E−14	43.89866	15.95407	0.286859	4.06E−02	1.80	0.25
960	13	1.62070	1.84E−02	4.95E−02	4.42E−03	3.74E−14	49.93377	17.4566	0.2861237	4.57E−02	1.79	0.29
1050	13	1.03478	1.82E−02	4.95E−02	2.47E−03	1.21E−13	69.52571	26.67936	0.2775867	1.54E−02	1.74	0.10
1150	13	0.68193	1.78E−02	4.95E−02	1.31E−03	1.78E−13	98.31142	38.73492	0.2656399	1.28E−02	1.66	0.08
1350	13	3.48398	2.31E−02	4.95E−02	8.84E−03	1.05E−14	99.99	23.76596	0.8435678	1.57E−01	5.28	0.98
AY9/2/99−2	Biotite	6.1 mg	J = 0.003472373							Location: 38°44′32.76″N, 75°10′25.86″E		
T (C)	t (min)	$^{40}Ar/^{39}Ar$	$^{38}Ar/^{39}Ar$	$^{37}Ar/^{39}Ar$	$^{36}Ar/^{39}Ar$	^{39}Ar (mol)	$\Sigma^{39}Ar$	$\%^{40}Ar^*$	$^{40}Ar^*/^{39}Ar_K$	$\pm\sigma_{40/39}$	Age (Ma)	$\pm\sigma_{Age}$
500	13	88.13135	2.26E−01	4.95E−02	3.07E−01	4.13E−15	0.7966194	−2.859436	−2.523757	5.64E+00	0.00	0.00
600	13	10.66066	6.38E−−02	4.95E−02	3.10E−02	9.30E−15	2.589696	13.59461	1.456948	2.21E−01	9.10	1.38
700	13	3.389266	5.70E−02	4.95E−02	8.81E−03	3.87E−14	10.05551	22.28004	0.7581571	4.98E−02	4.74	0.31
770	13	1.547356	5.58E−02	4.95E−02	2.49E−03	8.83E−14	27.08401	50.33478	0.7818579	2.53E−02	4.89	0.16
840	0	1.346868	5.45E−02	4.95E−02	1.79E−03	7.26E−14	41.08172	58.30873	0.7895573	1.72E−02	4.94	0.11
900	0	1.682693	5.40E−02	4.95E−02	2.94E−03	3.71E−14	48.23936	46.19348	0.7838089	2.94E−02	4.90	0.18
960	13	1.520969	5.55E−02	4.95E−02	2.44E−03	5.02E−14	57.91375	50.45228	0.7726329	3.58E−02	4.83	0.22
1050	13	1.144191	5.54E−02	4.95E−02	1.16E−03	1.43E−13	85.44038	67.36731	0.7732993	1.31E−02	4.84	0.08
1150	13	1.59641	5.38E−02	4.95E−02	2.30E−03	6.31E−14	97.61009	55.37663	0.8886437	3.09E−02	5.56	0.19
1350	15	6.297352	4.25E−02	4.95E−02	9.66E−03	1.24E−14	99.99	53.85843	3.414424	1.47E−01	21.3	0.9
AY9/3/99-1	Biotite	7.2 mg	J = 0.003460157							Location: 38°45′16.61″N, 75° 5′16.86″E		
T (C)	t (min)	$^{40}Ar/^{39}Ar$	$^{38}Ar/^{39}Ar$	$^{37}Ar/^{39}Ar$	$^{36}Ar/^{39}Ar$	^{39}Ar (mol)	$\Sigma^{39}Ar$	$\%^{40}Ar^*$	$^{40}Ar^*/^{39}Ar_K$	$\pm\sigma_{40/39}$	Age (Ma)	$\pm\sigma_{Age}$
500	0	85.6768	1.22E−01	4.95E−02	2.81E−01	7.03E−15	1.152326	2.964692	2.54319	4.56E+00	15.8	28.2
600	13	21.0010	3.27E−02	4.95E−02	6.96E−02	9.42E−15	2.69621	1.88868	0.3981055	2.99E−01	2.48	1.86
700	13	6.4487	1.87E−02	4.95E−02	2.10E−02	6.78E−14	13.81314	3.175353	0.2051145	5.95E−02	1.28	0.37
770	0	2.9874	1.48E−02	4.95E−02	9.19E−03	1.08E−13	31.573	8.096352	0.2424206	4.01E−02	1.51	0.25
840	13	2.1835	1.38E−02	4.95E−02	6.54E−03	7.27E−14	43.48223	10.11455	0.2218622	3.45E−02	1.38	0.22
880	13	3.3412	1.53E−02	4.95E−02	1.02E−02	3.25E−14	48.80661	8.876803	0.2985803	7.43E−02	1.86	0.46
920	13	3.5770	1.50E−−02	4.95E−02	1.12E−02	2.97E−14	53.67261	6.573951	0.2367602	7.85E−02	1.48	0.49
960	13	3.5403	1.48E−02	4.95E−02	1.10E−02	2.39E−14	57.59524	7.240262	0.2585254	9.53E−02	1.61	0.59
1000	13	3.1996	1.51E−02	4.95E−02	9.96E−03	3.38E−14	63.13146	7.05235	0.227163	8.07E−02	1.42	0.50
1070	13	1.9519	1.37E−02	4.95E−02	5.68E−03	9.13E−14	78.10128	12.467	0.2443427	2.70E−02	1.52	0.17
1150	13	1.6403	1.35E−02	4.95E−02	4.62E−03	1.12E−13	96.44817	14.89785	0.2453397	2.31E−02	1.53	0.14
1350	15	2.5997	1.56E−02	4.95E−02	6.16E−03	2.17E−14	99.99	28.53049	0.7512306	7.09E−02	4.68	0.44

interpreting higher temperature cooling age patterns that are the result of particles traveling along strain paths with different evolving thermal gradients.

4. Application to the Kongur Shan extensional system

4.1. Tectonic setting

The active Kongur Shan normal fault lies along the northeastern margin of the Pamir at the western end of the Himalayan–Tibetan orogenic belt (Fig. 8), and is part of a regional fault system which accommodates east–west extension in the hanging wall of the active Main Pamir Thrust (Arnaud et al., 1993; Brunel et al., 1994; Strecker et al., 1995; Blisniuk and Strecker, 1996; Robinson et al., 2004, 2007). The Main Pamir Thrust has been active since at least the Late Oligocene (Thomas et al., 1994; Sobel and Dumitru, 1997) and accommodates northward motion of the Pamir salient over the Tarim and Tajik basins (Burtman and Molnar, 1993; Brunel et al., 1994; Strecker et al., 1995; Arrowsmith and Strecker, 1999; Coutand et al., 2002). North-directed thrusting along the Main Pamir thrust has been interpreted to be related to east–west extension in the northern Pamir by either extensional collapse of over-thickened crust (Brunel et al., 1994) or radial thrusting along the Main Pamir Thrust (Strecker et al., 1995).

4.2. Kongur Shan normal fault

We focus on thermochronologic data collected from a transect across the footwall of the Kongur Shan normal fault along the northern flank of the Kongur Shan massif along the east-flowing Ghez river (Fig. 9A). Here the fault bounds the western flank of the Kongur Shan massif, dipping ~40° to the west (Fig. 9). Mylonitic fabrics along the western flank of the Kongur Shan massif show top-west sense of shear, consistent with the active east–west extension (Brunel et al., 1994; Robinson et al., 2004). Along the massif, the footwall appears to be a coherent geologic terrane with no evidence for hanging wall excisement by the Kongur Shan normal fault. Field studies of the hanging wall of the Kongur Shan normal fault indicate it behaved as an essentially rigid body with little or no internal deformation (Robinson et al., 2004). Additionally, except for a thin veneer of Quaternary glacial and fluvial deposits, there is no hanging wall basin development indicating little or no hanging wall subsidence.

The schists, gneisses, and deformed granites in the footwall of the Kongur Shan normal fault form a large antiformal dome with a north-northwest trending axis which plunges moderately to the north-northwest (Fig. 9) (Brunel et al., 1994; Robinson et al., 2004). The development of the domal structure of the Kongur Shan massif has been previously interpreted to be related to the development of a ramp anticline in the hanging wall of the Main Pamir Thrust (Brunel et al., 1994). Alternatively, the domal structure may be related to footwall rollover during east–west extension. The eastern side of the Kongur Shan massif is bounded by the steeply east dipping right-slip Ghez fault (Fig. 9). While earlier studies interpreted the structure to be a strike-slip fault (Brunel et al., 1994; Robinson et al., 2004), recent work suggests the Ghez fault may be a rotated sub-horizontal shear zone which was active immediately prior to initiation of east–west extension (Robinson et al., 2007) requiring 70°–80° of footwall rollover during exhumation.

4.3. Constraints on initial conditions

Petrologic and geochronologic studies from Robinson et al. (2004) along the northern flank of the Kongur Shan massif provide critical constraints on the initial conditions of the footwall immediately prior to initiation of east–west extension and exhumation along the Kongur Shan normal fault: (1) Thermobarometry from a footwall garnet–kyanite bearing schist directly below the fault surface (Fig. 9) yields peak metamorphic conditions of ~8 kbar, 700 °C, consistent with minimum pressure–temperature constraints from petrologic observations which show staurolite breaking down to kyanite + garnet. (2) In-situ ion-microprobe Th–Pb analyses of monazite inclusions in garnet yield a maximum age on the timing of peak metamorphic conditions of 9.2 Ma. Further, multi-diffusional domain (MDD) modeling of a K-feldspar $^{40}Ar/^{39}Ar$ analysis from a footwall sample taken ~35 km northwest of Kongur Shan dates initiation of extension along the northern portion of the extensional system at 7–8 Ma (Robinson et al., 2004). Together, these results indicate footwall rocks currently exposed directly below the fault have been exhumed from depths of ~30 km since the late Miocene due to slip along the Kongur Shan normal fault.

Further constraints on the pre-extensional geometry of the footwall are provided by a sample from the shear zone of the Ghez fault which contains syn-kinematic garnet (Fig. 9). As the Ghez shear zone is interpreted to have been active immediately prior to initiation of east–west extension (Robinson et al., 2007), it indicates pre-extension temperature conditions of ~450°–500 °C (depths of ~17–20 km) at distances of 16 km from the fault along the studied transect. This gradient of 1 km exhumation per 1.5–1.2 km of horizontal distance along the studied transect, similar to the gradient along a 40° dipping fault surface (1 km per 1.55 km along the fault), requires the Kongur Shan normal fault to have a roughly constant dip to a depth of at least 30 km.

One of the difficulties in assessing the structural evolution of metamorphic core complexes is the lack of unambiguous structural markers. While the Kongur Shan massif consists of several different lithologic units (two different metasedimentary units and Triassic orthogneisses), the original orientation of these units and the amount of rotation they have experienced is unclear. Thus, the current orientation of the Ghez fault and footwall foliations adjacent to the fault give us the best estimate on the amount of rollover of ~70°.

4.4. Kongur Shan massif cooling ages

Several studies have documented the rapid recent exhumation of the footwall of the Kongur Shan normal fault, yielding muscovite $^{40}Ar/^{39}Ar$ cooling ages as young as 1.8 Ma along the northwestern flank of the Kongur Shan massif (Arnaud et al., 1993; Robinson et al., 2004). Muscovite and biotite $^{40}Ar/^{39}Ar$ cooling ages combined with MDD modeling of K-feldspar $^{40}Ar/^{39}Ar$ analyses by Arnaud et al. (1993) documented a rapid increase in cooling rate at 1.5–2 Ma from ~50 °C/Ma to >100 °C/Ma which was interpreted to reflect an increase in exhumation rate. Alternatively, Robinson et al. (2004) suggested constant exhumation rates since initiation of extension at ~7–8 Ma based on MDD modeling of a K-feldspar analyses from a footwall sample ~35 km to the northwest.

We have integrated new biotite and muscovite $^{40}Ar/^{39}Ar$ analyses from the footwall for this study (Table 2, Fig. DR1) with the results from Robinson et al. (2004) in order to expand spatial coverage and incorporate data from both muscovite and biotite. All analyses are reported as inverse isochron ages except for the biotite analyzed from sample AY 8/29/99-6 which is reported as a weighted mean age due to the low concentration of radiogenic argon (1%–5% for most steps) (Table 2). All the analyzed samples come from near the bottom of a deeply incised valley (Fig. 9). However, the effect of the local topography (i.e. valley samples vs. ridge samples) on the position of the isotherms for the biotite and muscovite closure temperatures would be minimal due to the short wavelength of the valley (i.e. <10 km, Mancktelow and Grasemann, 1997; Braun, 2002). Thus the important aspect of the sample positions is their distance from the detachment surface which increases to the east (Fig. 9B). A plot of cooling age variation with distance from the fault (Fig. 10) shows three important features: (1) Muscovite ages increase gradually with distance from the fault over ~10 km from 1.8 to 2.8 Ma. Biotite age data is sparser but show a broadly similar pattern with a gradual increase in age from 1.2 to 1.6 Ma.

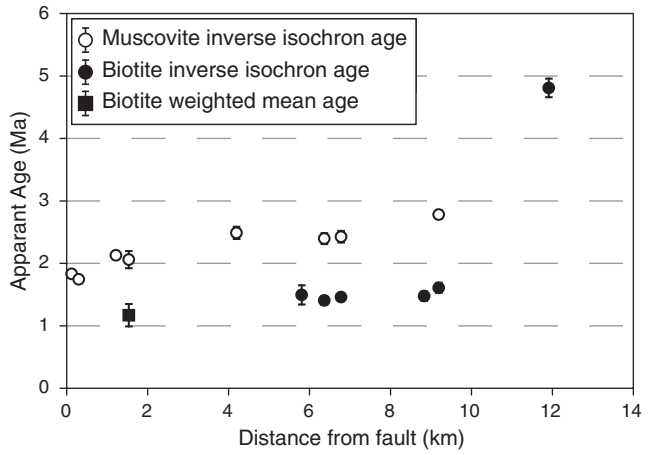

Fig. 10. $^{40}Ar/^{39}Ar$ apparent age vs. distance from the surface exposure of the Kongur Shan normal fault.

(2) Over the first 10 km, biotite ages are consistently younger than muscovite ages by ~1 Ma. (3) Biotite ages increase sharply at ~12 km from the fault from 1.5 Ma to 4.8 Ma.

The cooling age pattern and constraints on the magnitudes of exhumation present several interesting relationships which provide information on the cooling and exhumation history of the footwall of the Kongur Shan normal fault: (1) Young biotite and muscovite ages from the footwall require rapid cooling (>150 °C/Ma) during the past 1–2 Ma, as noted by Arnaud et al. (1993). (2) The consistency in age of the muscovite and biotite analyses over the first 10 km of the footwall transect indicate large portions of the footwall sampled in this study cooled through the respective closure temperatures at roughly the same time. (3) The consistent 1 Ma spread in cooling ages between the biotite and muscovite analyses requires cooling rates of ~100 °C/Ma during passage through the relative isotherms. (4) P–T–t data from the footwall requires an average cooling rate of 80°–90 °C/Ma since initiation of extension at ~8 Ma.

4.5. Modeling cooling age patterns from the Kongur Shan massif

In order to simulate the age distribution observed in the footwall of the Kongur Shan normal fault, we used the model of a sub-vertical simple shear rolling hinge incorporating erosion of the footwall during exhumation. This model was chosen because; (1) the transect is along a deeply incised portion of the footwall with local relief indicating a minimum of 4 km of erosion (Fig. 9), and (2) the magnitude of exhumation from samples directly below the fault and the distance to lower-grade footwall rocks exposed to the east require a continuously decreasing pressure gradient of exposed footwall rocks rather than the broad region of similar pressures that result from our flexural rolling hinge model with coupled erosion. While a more realistic flexural rolling hinge model would likely result in a similar continuous decrease in footwall pressure, the minor difference in kinematics would not change our conclusions.

In our exploration of modeled cooling age patterns we use a fault dip of 40° and a width of the zone of erosion, *d*, of 10 km, and varying magnitudes of exhumation (30 km, 27.5 km, and 25 km). This yields a final footwall metamorphic gradient similar to that observed, with samples 15 km from the fault starting at depths of ~16–20 km. We explored the effect of variations in the timing and duration of slip rates in matching the observed cooling age patterns, focusing on: (1) the 1 Ma spread in ages between the muscovite and biotite analyses, (2) the 10 km zone of slowly increasing mica ages, and to a lesser extent (3) the sharp inflection in biotite ages between distances of 10 and 13 km from the fault.

Models which begin exhumation at 8 Ma from different depths with a constant fault slip rate (Fig. 11A) successfully reproduce the ~1 Ma spread in ages between the muscovite and biotite ages. However, constant exhumation rates since 8 Ma beginning at depths of 27.5 and 25 km produce ages that are too old by ~0.5 and 1 Ma respectively due to the slow exhumation rates (3.1 mm/yr and 3.5 mm/yr respectively). Model results using an initial depth of 30 km and a slip rate of 5.85 mm/yr produce a reasonably good fit to the analytical data, but the predicted biotite ages tend to be slightly older than observed. Importantly, all sample cooling histories from these models (Fig. 11B) show an increase in cooling rate at 2–3 Ma from ~45 °C/Ma to ~200 °C/Ma. This is due to; 1) the rapid advection of isotherms during the early stages of exhumation resulting in slow cooling of deep portions of normal fault footwalls, followed by 2) rapid cooling as particles are advected through the highly compressed isotherms which begin to approach steady state. The increase in cooling rate is similar to that reported by Arnaud et al. (1993), although it begins ~1 Ma sooner.

Models which use a constant slip rate of 6.5 mm/yr (exhumation rate of 4.2 mm/yr) beginning at different depths all result in reasonably good fits to the analytical data, reproducing both the muscovite and biotite absolute ages, as well as the ~1 Ma spread between the muscovite and biotite ages (Fig. 11C). Initiation ages for these models of 7.2 Ma, 6.6 Ma, and 6 Ma for initial depths of 30, 27.5, and 25 km respectively are on the lower end of that predicted by K-feldspar MDD modeling results from Robinson et al. (2004), but are generally consistent with the interpreted initiation of extension at ~7–8 Ma. Cooling histories from these models show a similar cooling history with T–t paths from all models converging ~2 Ma. Importantly, these models show an increase in cooling rate at ~2 Ma from ~45–50 °C/Ma to ~200 °C/Ma, consistent with the results from Arnaud et al. (1993).

5. Discussion of Kongur Shan modeling results

Our modeling of the cooling age patterns of the Kongur Shan massif yields several important results both for understanding the evolution of the Kongur Shan normal fault, as well as interpreting cooling ages from deeply exhumed detachment fault footwalls. One interesting aspect to note is that the model results show that the observed cooling age pattern is relatively insensitive to duration of exhumation (e.g. 7.2 Ma vs. 6 Ma, Fig. 11C) and is much more sensitive to exhumation rate. This is in part due to the parameters that we are trying to address, where particles from depths that we are interested in reach the relevant isotherms (i.e. closure temperatures) when the rate of isotherm advection has slowed significantly. The isotherms are thus at roughly the same depth regardless of how long the model has been running. At distances further from the fault than we have data for (i.e. 15 to 20 km), modeled ages begin to diverge where particles were exhumed through the closure temperatures when isotherm advection was still relatively rapid.

As discussed above, initial conditions from previous integrated thermobarometry, monazite Th–Pb geochronology, and $^{40}Ar/^{39}Ar$ cooling ages require high-grade rocks in the footwall of the Kongur Shan normal fault to have undergone an increase in cooling rate from ~50 °C/Ma prior to 3 Ma to ~200 °C/Ma from 2 Ma to present. While previous studies related this dramatic Late Pliocene increase in cooling rate to an increase in exhumation rate (Arnaud et al., 1993), our modeling results show that the increase in cooling rate can be produced by a constant exhumation rate. Models which use a two stage slip/exhumation history with an increase at 2 Ma (Fig. 11E and F) as proposed by Arnaud et al. (1993) generally result in modeled muscovite and biotite ages which are too young (e.g. 1.5 and 1 Ma respectively, Fig. 11E), as well as too little difference between the muscovite and biotite ages. While the results presented are non-unique, and it is likely that one could produce the observed cooling age pattern using a two stage history, a fit using a constant exhumation rate argues against a change in kinematics during

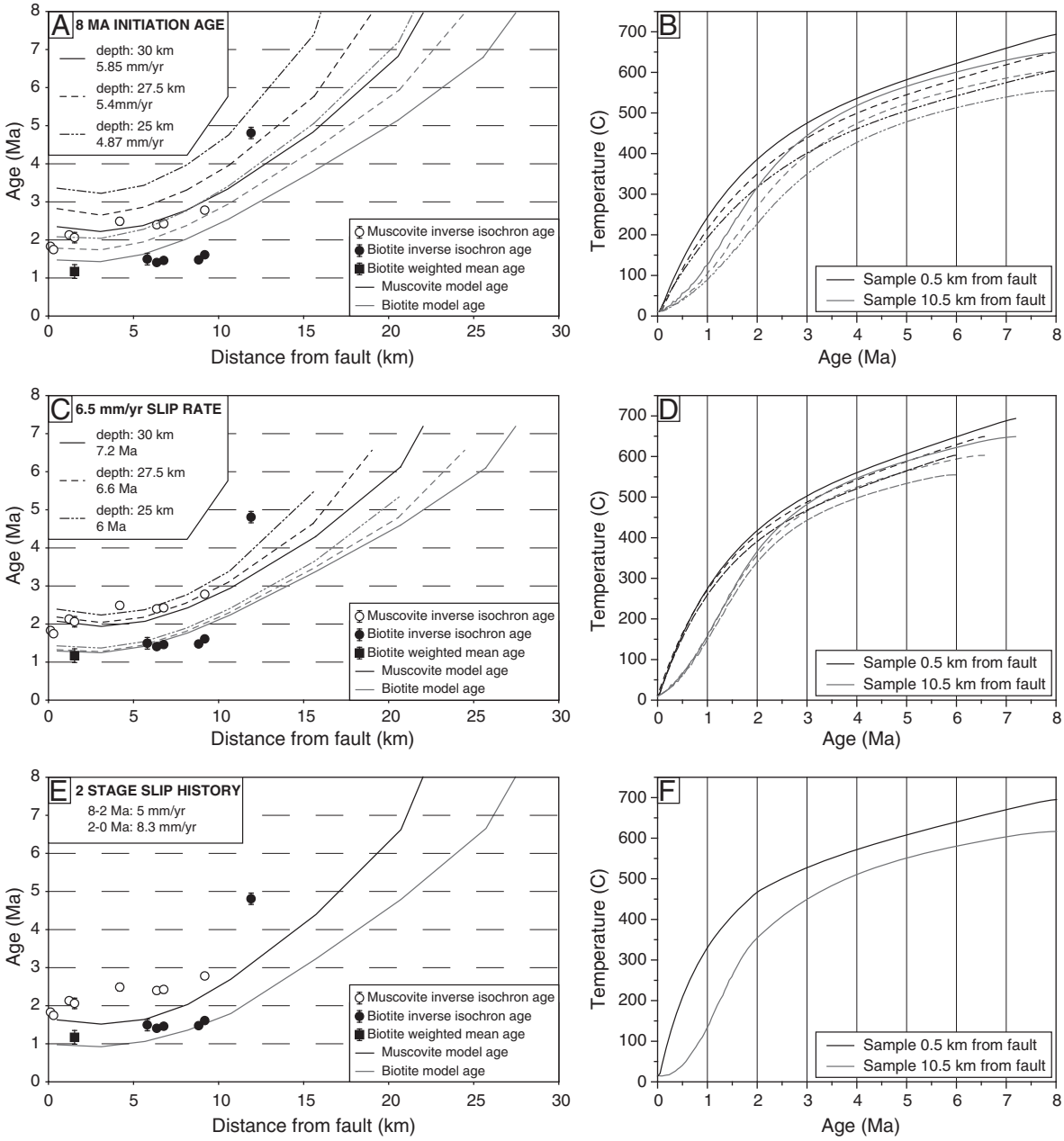

Fig. 11. Modeled and observed muscovite and biotite age patterns and modeled T–t paths for different kinematic scenarios. The limit of the cooling age curves is the limit of particles that were above the muscovite and biotite closure temperatures prior to deformation. (A) and (B) Slip starting at 8 Ma from different depths with different slip rates. (C) and (D) Slip rate of 6.5 mm/yr starting at different depths with different initiation ages. (E) and (F) Two-stage slip rate history starting at 8 Ma: Slip rate of 5 mm/yr for 6 Ma followed by slip rate of 8.3 mm/yr for 2 Ma.

the Late Pliocene. These results are consistent with the interpretation that exhumation has been constant since initiation of extension based on K-feldspar MDD modeling from a less exhumed portion of the footwall (Robinson et al., 2004).

Two minor aspects of the analytical data were not accurately reproduced. First, the sharp inflection point in the cooling ages was not matched. However, as mentioned previously, the inflection is based on a single sample which is possibly affected by excess ^{40}Ar as younger muscovite ages have been obtained to the southeast of our transect (Arnaud et al., 1993). A second order feature present in the analytical data but not reproduced is a small increase in muscovite cooling ages over the first 1.2 km from the fault. Instead, the modeled cooling ages actually show a slight drop in cooling age over the first couple of km. This is likely due to the simplified kinematics of the model which doesn't take into account the distribution of shear in the footwall during extension as evidenced by the thick mylonitic shear zone.

An important aspect to emphasize is the role of erosion of footwall material during exhumation on the observed cooling age pattern. If one used a simple relationship of age vs. distance from the fault to calculate a slip rate on the fault, the relatively slow increase in muscovite cooling ages over the first 10 km would result in unreasonably high calculated slip rates of 10–15 mm/yr. Taking erosion into account allows large portions of the presently exposed footwall to have passed through a given isotherm (i.e. closure temperature) at the same time resulting in the relatively flat age vs. distance relationship observed at Kongur Shan.

Another interesting result from this study is that there is no evidence for Late Pliocene to Recent enhanced glacial erosion influencing the cooling history of the Kongur Shan massif for the high temperature

thermochronometers evaluated here. However, it is possible that taking into account isostatically driven uplift/exhumation due to rapid glacial erosion may result in a slightly better fit to the analytical results. Isostatically driven uplift and exhumation during rapid glacial erosion may also yield a better fit to structural observations. As discussed previously, the limited constraints we have suggest ~70°–80° of footwall rotation at the Ghez fault. Our simplified kinematic model results in maximum footwall rotation equal to the dip of the fault (i.e. 40° in the Kongur Shan model runs). Enhanced isostatic driven uplift of the Kongur Shan massif would potentially yield a better fit to the limited structural observations.

6. Conclusions

(1) Deeply eroded detachment fault footwalls preserve distinct concave cooling age vs. distance patterns for higher temperature thermochronometers due to footwall particles being advected through higher thermal gradients with greater distance from the active detachment surface. These results are similar to the effects on low-temperature thermochronometers in footwalls of normal faults experiencing footwall erosion (e.g. Ehlers et al., 2001).

(2) Based on previously determined initial conditions from geochronologic and thermobarometric studies, cooling ages along Kongur Shan massif in the eastern Pamir can be modeled as the result of a constant slip/exhumation rate on the Kongur Shan normal fault of 6.5/4.2 mm/yr since ~7 Ma if erosion of footwall material is taken into account. Although modeled cooling histories match the dramatic increase in cooling rate at ~2 Ma reported by Arnaud et al. (1993), these results show that east–west extension on the Kongur Shan normal fault has likely been constant since initiation of extension at 7–8 Ma as suggested by Robinson et al. (2004).

Supplementary materials related to this article can be found online at doi:10.1016/j.tecto.2010.10.003.

Acknowledgments

We thank an anonymous reviewer, Fabrizio Storti, and Jean-Phillipe Avouac whose careful and thorough comments significantly improved this paper, and Ed Sobel whose careful and critical review of an earlier version of this manuscript improved the presentation of the ideas. Special thanks to Stewart Hall for assistance in plotting the isotherm results. This work was partially supported by National Science Foundation grant EAR-0126122 and EAR-0911598.

References

Arnaud, N.O., Brunel, M., Cantagrel, J.M., Tapponnier, P., 1993. High cooling and denudation rates at Kongur Shan, eastern Pamir (Xinjiang, China) revealed by $^{40}Ar/^{39}Ar$ alkali feldspar thermochronology. Tectonics 12, 1335–1346.

Arrowsmith, J.R., Strecker, M.R., 1999. Seismotectonic range-front segmentation and mountain-belt growth in the Pamir-Alai region, Kyrgyzstan (India–Eurasia collision zone). GSA Bulletin 111, 1665–1683.

Axen, G.J., Bartley, J.M., 1997. Field tests of rolling hinges: existence, mechanical types, and implications for extensional tectonics. Journal of Geophysical Research 102, 20,515–20,537.

Beaumont, C., Jamieson, R.A., Nguyen, M.H., Lee, B., 2001. Himalayan tectonics explained by extrusion of a low-viscosity crustal channel coupled to focused surface denudation. Nature 414, 738–742.

Blisniuk, P.M., Strecker, M.R., 1996. Kinematics of Holocene normal faulting in the Northern Pamir. Eos, Transactions, American Geophysical Union 77, F693.

Brady, R.J., 2002. Very high slip rates on continental extensional faults: new evidence from (U–Th)/He thermochronometry of the Buckskin Mountains, Arizona. Earth and Planetary Science Letters 197, 95–104.

Braun, J., 2002. Quantifying the effect of recent relief changes on age-elevation relationships. Earth and Planetary Science Letters 200, 331–343.

Brichau, S., Ring, U., Carter, A., Bolhar, R., Monié, P., Stockli, D., Brunel, M., 2008. Timing, slip rate, displacement and cooling history of the Mykonos detachment footwall, Cyclades, Greece, and implications for the opening of the Aegean Sea basin. Journal of the Geological Society 165, 263–277.

Brunel, M., Arnaud, N., Tapponnier, P., Pan, Y., Wang, Y., 1994. Kongur Shan normal fault: type example of mountain building assisted by extension (Karakoram fault, eastern Pamir). Geology 22, 707–710.

Buck, W.R., 1988. Flexural rotation of normal faults. Tectonics 7, 959–973.

Buck, W.R., Martinez, F., Steckler, M.S., Cochran, J.R., 1988. Thermal consequences of lithospheric extension: pure and simple. Tectonics 7, 213–234.

Burbank, D.W., Blythe, A.E., Putkonen, J., Pratt-Sitaula, B., Gabet, E., Oskin, M., Barros, A., Ojha, T.P., 2003. Decoupling of erosion and precipitation in the Himalayas. Nature 426, 652–655.

Burtman, V.S., Molnar, P., 1993. Geological and geophysical evidence for deep subduction of continental crust beneath the Pamir. Geological Society of America Special Paper 281, 76.

Carter, T.J., Kohn, B.P., Foster, D.A., Gleadow, A.J.W., 2004. How the Harcuvar Mountains metamorphic core complex became cool: evidence from apatite (U–Th)/He thermochronometry. Geology 32, 985–988.

Carter, T.J., Kohn, B.P., Foster, D.A., Gleadow, A.J.W., Woodhead, J.D., 2006. Late-stage evolution of the Chemehuevi and Sacramento detachment faults from apatite (U–Th)/He thermochronometry—evidence for mid-Miocene accelerated slip. Geological Society of America Bulletin 118, 689–709.

Cogan, M.P., Nelson, K.D., Kidd, W.S.F., Wu, C.D., 1998. Shallow structure of the Yadong-Gulu rift, southern Tibet, from refraction analysis of Project INDEPTH common midpoint data. Tectonics 17, 46–61.

Coutand, I., Strecker, M.R., Arrowsmith, J.R., Hilley, G., Thiede, R.C., Korjenkov, A., Omuraliev, M., 2002. Late Cenozoic tectonic development of the intramontane Alai Valley, (Pamir-Tien Shan region, central Asia): an example of intracontinental deformation due to the Indo-Eurasia collision. Tectonics 21, 1051. doi:10.1029/2002TC001358.

Davis, G.A., Lister, G.S., 1988. Detachment faulting in continental extension: perspectives from the southwestern U.S. Cordillera. Geological Society of America Special Paper 218, 133–159.

Ehlers, T.A., Farley, K.A., 2003. Apatite (U–Th)/He thermochronometry: methods and applications to problems in tectonic and surface processes. Earth and Planetary Science Letters 206, 1–14.

Ehlers, T.A., Armstrong, P.A., Chapman, D.S., 2001. Normal fault thermal regimes and the interpretation of low-temperature thermochronometers. Physics of the Earth and Planetary Interiors 126, 179–194.

Ehlers, T.A., Willet, S.D., Armstrong, P.A., Chapman, D.S., 2003. Exhumation of the central Wasatch Mountains, Utah: 2. Thermokinematic model of exhumation, erosion, and thermochronometer interpretation. Journal of Geophysical Research 108 (2173). doi:10.1029/2001JB001723.

Foster, D.A., John, B.E., 1999. Quantifying tectonic exhumation in an extensional orogen with thermochronology: examples from the southern Basin and Range province. In: Willett, S.D. (Ed.), Exhumation Processes: Normal Faulting, Ductile Flow and Erosion: Geological Society, London, Special Publications, 154, pp. 343–364.

Friedmann, S.J., Burbank, D.W., 1995. Rift basins and supradetachment basins: intracontinental extensional end members. Basin Research 7, 109–127.

Giovanni, M.K., Horton, B.K., Garzione, C.N., McNulty, B. and Grove, M., (in press). Extensional basin evolution in the Cordillera Blanca, Peru: Stratigraphic and isotopic records of detachment faulting and orogenic collapse in the Andean hinterland, Tectonics. doi:10.1029/2010TC002666.

Grasemann, B., Mancktelow, N.S., 1993. Two-dimensional thermal modelling of normal faulting: the Simplon Fault Zone, Swiss Alps, Switzerland. Tectonophysics 225, 155–165.

Grove, M., Harrison, T.M., 1996. $^{40}Ar^{*}$ diffusion in Fe-rich biotite. American Mineralogist 81, 940–951.

Harrison, T.M., Duncan, I., McDougall, I., 1985. Diffusion of ^{40}Ar in biotite: temperature, pressure and compositional effects. Geochimica et Cosmochimica Acta 49, 2461–2468.

Harrison, T.M., Copeland, P., Kidd, W.S.F., Lovera, O.M., 1995. Activation of the Nyainquentanghla Shear Zone: implications for uplift of the southern Tibetan Plateau. Tectonics 14, 658–676.

Harrison, T.M., Célérier, J., Aikman, A.B., Hermann, J., Heizler, M.T., 2009. Diffusion of ^{40}Ar in muscovite. Geochimica et Cosmochimica Acta 73, 1039–1051.

John, B.E., Foster, D.A., 1993. Strucutral and thermal constraints of the initiation angle of detachment faulting in the Southern Basin and Range: the Chemehuevi Mountains case study. Geological Society of America Bulletin 105, 1091–1108.

Kapp, J.L.D.A., Harrison, T.M., Kapp, P., Grove, M., Lovera, O.M., Lin, D., 2005. Nyainqentanglha Shan: a window into the tectonic, thermal, and geochemical evolution of the Lhasa block, southern Tibet. Journal of Geophysical Research 110. doi:10.1029/2004JB003330.

Ketcham, R.A., 1996. Thermal models of core-complex evolution in Arizona and New Guinea: implications for ancient cooling paths and present-day heat flow. Tectonics 15, 933–951.

Lister, G.S., Davis, G.A., 1989. The origin of metamorphic core complexes and detachment faults formed during Tertiary continental extension in the northern Colorado River region, U.S.A. Journal of Structural Geology 11, 65–94.

Mancktelow, N.S., Grasemann, B., 1997. Time-dependant effects of heat advection and topography on cooling histories during erosion. Tectonophysics 270, 167–195.

Manning, A.H., Bartley, J.M., 1994. Postmylonitic deformation in the Raft River metamorphic core complex, northwestern Utah: evidence of a rolling hinge. Tectonics 13, 596–612.

McDougall, I., Harrison, T.M., 1999. Geochronology and Thermochronology by the $^{40}Ar/^{39}Ar$ Method. Oxford University Press, New York. 269 pp.

Moore, M.A., England, P.C., 2001. On the inference of denudation rates from cooling ages of minerals. Earth and Planetary Science Letters 185, 265–284.

Murphy, M.A., Yin, A., Kapp, P., Harrison, T.M., Manning, C.E., Ryerson, F.J., Lin, D., Jinghui, G., 2002. Structural evolution of the Gurla Mandhata detachment system, southwest Tibet: implications for the eastward extent of the Karakoram fault system. Geological Society of America Bulletin 114, 428–447.

Pan, Y., Kidd, W.S.F., 1992. Nyainqentanglha shear zone: a late Miocene extensional detachment in the southern Tibetan plateau. Geology 20, 775–778.
Reiners, P.W., Brandon, M.T., 2006. Using thermochronology to understand orogenic erosion. Annual Review of Earth and Planetary Sciences 34, 419–466.
Richard, S.M., Fryxell, J.E., Sutter, J.F., 1990. Tertiary structure and thermal history of the Harquahala and Buckskin mountains, west central Arizona: implications for denudation by a major detachment fault system. Journal of Geophysical Research 95, 19,973–19,987.
Robinson, A.C., Yin, A., Manning, C.E., Harrison, T.M., Zhang, S.-H., Wang, X.-F., 2004. Tectonic evolution of the northeastern Pamir: constraints from the northern portion of the Cenozoic Kongur Shan extensional system. Geological Society of America Bulletin 116, 953–974.
Robinson, A.C., Yin, A., Manning, C.E., Harrison, T.M., Zhang, S.-H., Wang, X.-F., 2007. Cenozoic evolution of the eastern Pamir: implications for strain-accommodation mechanisms at the western end of the Himalayan–Tibetan orogen. Geological Society of America Bulletin 7/8, 882–896.
Ruppel, C., Royden, L., Hodges, K.V., 1988. Thermal modeling of extensional tectonics: applications to pressure–temperature–time histories of metamorphic rocks. Tectonics 7, 947–957.
Sobel, E.R., Dumitru, T.A., 1997. Thrusting and exhumation around the margins of the western Tarim basin during the India–Asia collision. Journal of Geophysical Research 102, 5043–5063.
Spencer, J., 1984. Role of tectonic denudation in warping and uplift of low-angle normal faults. Geology 12, 95–98.
Strecker, M.R., Frisch, W., Hamburger, M.W., Ratschbacher, L., Semiletkin, S., Zamoruyev, A., Sturchio, N., 1995. Quaternary deformation in the Eastern Pamirs, Tadzhikistan and Kyrgyzstan. Tectonics 14, 1061–1079.
Suppe, J., Medwedeff, D.A., 1990. Geometry and kinematics of fault-propagation folding. Eclogae Geologicae Helvetiae 83, 409–454.
Thomas, J.-C., Chauvin, A., Gapais, D., Bazhenov, M.L., Perroud, H., Cobbold, P.R., Burtman, V.S., 1994. Paleomagnetic evidence for Cenozoic block rotations in the Tadjik depression (Central Asia). Journal of Geophysical Research 99, 15141–15160.
Turcotte, D.L., Schubert, G., 2002. Geodynamics. Cambridge University Press. 450 pp.
Webb, A.A.G., Yin, A., Harrison, T.M., Célérier, J., Burgess, W.P., 2007. The leading edge of the Greater Himalayan Crystalline complex revealed in the NW Indian Himalaya: implications for the evolution of the Himalayan orogen. Geology 35, 955–958.
Wells, M.L., Snee, L.W., Blythe, A.E., 2000. Dating of major normal fault systems using thermochronology: an example from the Raft River detachment, Basin and Range, western United States. Journal of Geophysical Research 105, 16,303–16,327.
Wernicke, B., Axen, G.J., 1988. On the role of isostasy in the evolution of normal fault systems. Geology 16, 848–851.
Xiao, H., Suppe, J., 1992. Origin of rollover. American Association of Petroleum Geologists Bulletin 76, 509–529.
Yin, A., 2004. Gneiss domes and gneiss dome systems. In: Siddoway, C.S. (Ed.), Gneiss domes in orogeny: Geological Society of America Special Paper, 380, pp. 1–14.
Yin, A., 2006. Cenozoic tectonic evolution of the Himalayan orogen as constrained by along-strike variation of structural geometry, exhumation history, and foreland sedimentation. Earth Science Reviews 76, 1–131.
Yin, A., Dunn, J.F., 1992. Structural and stratigraphic development of the Whipple–Chemehuevi detachment fault system, southeastern California: implications for the geometrical evolution of domal and basinal low-angle normal faults. Geological Society of America Bulletin 104, 659–674.
Yin, A., Harrison, T.M., 2000. Geologic evolution of the Himalayan–Tibetan Orogen. Annual Review of Earth and Planetary Sciences 28, 211–280.
Zeitler, P.K., Koons, P.O., Bishop, M.P., Chamberlain, C.P., Craw, D., Edwards, M.A., Hamidullah, S., Janm, M.Q., Khan, M.A., Khattak, M.U.K., Kidd, W.S.F., Mackie, R.L., Meltzer, A.S., Park, S.K., Pêcher, A., Poage, M.A., Sarker, G., Schneider, D.A., Seeber, L., Shroder, J.F., 2001. Crustal reworking at Nanga Parbat, Pakistan: metamorphic consequences of thermal–mechanical coupling facilitated erosion. Tectonics 20, 712–728.